2019

Hot-Wire Anemometer Measurements of Atmospheric Surface Layer Turbulence via Unmanned Aerial Vehicle

Caleb A. Canter
University of Kentucky, caleb.canter@uky.edu
Digital Object Identifier: https://doi.org/10.13023/etd.2019.341

Right click to open a feedback form in a new tab to let us know how this document benefits you.

STUDENT AGREEMENT:

I represent that my thesis or dissertation and abstract are my original work. Proper attribution has been given to all outside sources. I understand that I am solely responsible for obtaining any needed copyright permissions. I have obtained needed written permission statement(s) from the owner(s) of each third-party copyrighted matter to be included in my work, allowing electronic distribution (if such use is not permitted by the fair use doctrine) which will be submitted to UKnowledge as Additional File.

I hereby grant to The University of Kentucky and its agents the irrevocable, non-exclusive, and royalty-free license to archive and make accessible my work in whole or in part in all forms of media, now or hereafter known. I agree that the document mentioned above may be made available immediately for worldwide access unless an embargo applies.

I retain all other ownership rights to the copyright of my work. I also retain the right to use in future works (such as articles or books) all or part of my work. I understand that I am free to register the copyright to my work.

REVIEW, APPROVAL AND ACCEPTANCE

The document mentioned above has been reviewed and accepted by the student's advisor, on behalf of the advisory committee, and by the Director of Graduate Studies (DGS), on behalf of the program; we verify that this is the final, approved version of the student's thesis including all changes required by the advisory committee. The undersigned agree to abide by the statements above.

<div align="right">

Caleb A. Canter, Student

Dr. Sean C. Bailey, Major Professor

Dr. Alexandre Martin, Director of Graduate Studies

</div>

Hot-Wire Anemometer Measurements of Atmospheric Surface Layer
Turbulence via Unmanned Aerial Vehicle

THESIS

A thesis submitted in partial fulfillment of the
requirements for the degree of Master of Science in
Mechanical Engineering in the College of Engineering
at the University of Kentucky

by

Caleb A. Canter

University of Kentucky

Director: Dr. Sean C. Bailey, Associate Professor of Mechanical
Engineering

Lexington, Kentucky

2019

ABSTRACT OF THESIS

Hot-Wire Anemometer Measurements of Atmospheric Surface Layer Turbulence via
Unmanned Aerial Vehicle

An instrumented unmanned aerial vehicle (UAV) was developed and employed to observe the full range of turbulent motions that exist within the inertial subrange of atmospheric surface layer turbulence. The UAV was host to a suite of pressure, temperature, humidity, and wind sensors which provide the necessary data to calculate the variety of turbulent statistics that characterize the flow. Flight experiments were performed with this aircraft, consisting of a large square pattern at an altitude of 100 m above ground level. In order to capture the largest turbulent scales it was necessary to maximize the size of the square pattern. The smallest turbulent scales, on the other hand, were measured through the use of a fast response constant temperature hot wire anemometer. The results demonstrates that the UAV system is capable of directly measuring the full inertial subrange of the atmospheric surface layer with high resolution and allowing for the turbulence dissipation rate to be calculated directly.

Caleb A. Canter
July 31, 2019

Hot-Wire Anemometer Measurements of Atmospheric Surface Layer Turbulence via Unmanned Aerial Vehicle

by

Caleb A. Canter

Dr. Sean C. Bailey
_____
Director of Thesis

Dr. Alexandre Martin,
_____
Director of Graduate Studies

July 31, 2019
_____

Acknowledgments

I would like to take this opportunity to thank my advisor, Dr. Sean Bailey for his continuous support in throughout my entire academic career at the University of Kentucky. He has gone above and beyond to help me become the capable engineer I am today.

I want to say thank you to my wife Kate Canter, and my family. They have been extremely supportive throughout my entire educational career.

I am extremely thankful for everyone who was involved in the UAV lab over the past 6 years. You have all been a tremendous help to me and it has been a pleasure working with you.

I would also like to thank Mike Thamann and Brandon Witte for their work in developing the previous BLUECAT airframes. Without this work in laying the foundation of the BLUECAT system none of this would be possible.

Table of Contents

List of Figures

Nomenclature

$[.]_A$	Denotes aerodynamic frame of reference
$[.]_B$	Denotes body fixed frame of reference
$[.]_I$	Denotes inertial frame of reference
α	Angle of attack
β	Angle of sideslip
η	Kolmogrov length scale
μ	Dynamic Viscosity
Ω_{UAV}	Angular velocity of UAV
$\overline{\zeta}$	Time averaged fluid property
ϕ	Angle of wind with respect to North
ρ	Density
τ_K	Kolmogrov time scale
τ_w	Shear stress
Θ	Potential temperature
ζ'	Time-varying fluctuations of fluid property
$\zeta(t)$	Arbitrary time-dependent fluid property

C_α Calibration coefficient for angle of attack

C_β Calibration coefficient for angle of sideslip

C_q Calibration coefficient for dynamic pressure

D Normalization factor for transformation

K Von Karmen Constant

k Turbulent kinetic energy

k^* Modified turbulent kinetic energy

$L_{i,j}$ Coordinate transformation matrix where i,j denote frame of reference

P Total pressure

p Local atmospheric pressure

p_0 Standard atmospheric pressure

P_{dyn} Dynamic pressure

r_{s-CG} Vector pointing from center of gravity to measurement volume on UAV

r_{UAV} Translational position of UAV

Re Reynolds Number

RH Relative humidity

T Temperature

t_i Time corresponding to each discrete sample of five-hole probe velocity

U Mean velocity

u x/East-West directional velocity $u = W_1$

u_τ	Shear velocity
u_i	ith component of the velocity vector
U_r	Relative velocity
U_S	Velocity of sensing volume
U_{UAV}	Velocity of UAV
v	y/North-South directional velocity $v = W_2$
V_i	Voltage corresponding to component u_i
v_K	Kolmogrov velocity scale
W	Wind velocity
w	z/up-down directional velocity $w = W_3$
x_i	ith component of the position vector
ABL	Atmospheric boundary layer
L	Length scale
TAS	True arispeed
UAV	Unmanned aerial vehicle

Chapter 1   Introduction

Humans experience the effects of turbulent flows every single day. Whether it's feeling an airplane rumble on a flight or simply stirring a hot cup of coffee, turbulent flows are an important part of the world around us. As a result, turbulent flows have been an active area of research in fluid mechanics for over a century, although it is often claimed that the earliest studies of turbulence were performed by Leonardo da Vinci [1] in his sketches capturing the eddies and whorls produced by a stream of water entering a tank.

One of the earliest significant results in the study of turbulence were achieved by Osborne Reynolds, who approached turbulence statistically through what is referred to as Reynolds decomposition [2]. However, this approach introduced more unknowns than there were governing equations, i.e. the closure problem, which prevents an exact solution using this approach and introduces the need to implement approximate models to describe turbulence. This was the case until recent years, when massive improvements in computational power made direct solution of the governing equations possible by bypassing the statistical approach and solving the discretized governing equations for all spatial and temporal turbulent scales. However, solving these equations numerically at a resolution sufficient to resolve all the turbulent scales is extremely computationally expensive and currently intractable for the majority of practical problems.

This computational challenge increases as a result of increasing the Reynolds number [3]. The Reynolds number is an important non-dimensional parameter for fluid

flows, describing the ratio between the inertial and viscous effects present in a fluid flow [4] and can be extended to the description of the ratio between the largest and smallest scales of the turbulence within the flow. There is particular academic interest in turbulence at high Reynolds number flows because when the scale separation becomes large enough, the smallest turbulence scales behave independently of the large scale fluctuations. This creates the possibility of developing a universal characterization of the fine structure turbulence in high Reynolds number flows [5]. However, most laboratory experiments are unable to produce flows with a high enough Reynolds number to create this condition, since the inertia of the flow depends on its velocity and length scale. Hence, wind tunnels, for example, limit the Reynolds number through the size and velocity of the wind tunnel or test chamber. There are facilities capable of producing a high Reynolds number by manipulating the density and viscosity of the flow, such as the Princeton Superpipe facility [6–8], but these facilities are relatively rare and produce their own diagnostic challenges.

On the other hand, the atmospheric boundary layer is one of the highest Reynolds number turbulence flows on Earth, and it is readily available and free to access. The atmospheric boundary layer can be defined as the lower part of the troposphere which is directly influenced by the Earth's surface, responding to surface forces with time scales of approximately one hour [9]. The atmospheric boundary layer is where all of the Earth's mass, momentum, and energy exchange with the atmosphere occurs, and turbulence is the means by which that mass, momentum, and energy is distributed throughout the rest of the atmosphere. Therefore, measuring the turbulence in the atmospheric boundary layer could not only help provide a universal characterization of the fine structure of high Reynolds number turbulence, it could also offer valuable insight into the formation and dissipation of many atmospheric events.

Historically, measurements of the atmospheric boundary layer were taken using tower or balloon-based sensors [10, 11]. These systems both have a few significant

drawbacks, including their lack of portability and their heavy reliance on Taylor's frozen flow hypothesis [12]. Taylor's hypothesis assumes that the structure of the turbulence does not evolve, or is 'frozen', as it advects past a stationary sensor, allowing measurements in the time domain to be transferred into the spatial domain through the average velocity of the flow past the sensor. This hypothesis is generally applicable when the time it takes for a turbulent eddy to advect past a sensor is short compared to the lifetime of the given eddy.

Higgins [13] studied the applicability of this hypothesis in the atmospheric boundary layer and found it to be acceptable for the small scale eddies that move past the sensor rather quickly, however this hypothesis does not extend to the larger eddies which tend to break down or change in the time it takes for them to fully advect past the sensor. In addition, eddies of different scale do not advect past the sensor at the same velocity, introducing bias in spatial spectra inferred from temporal measurements [14].

Instrumented manned aircraft are often used to measure atmospheric properties [15–21]. This approach does offer some advantage over tower-based sensors by reducing the reliance on Taylor's hypothesis, and allowing measurements over large spatial domains. However, manned aircraft are expensive to operate and conducting measurements at altitudes low enough to the ground to observe the boundary layer processes can be hazardous.

In recent years a new platform for measuring the atmospheric boundary layer has emerged. Unmanned aerial vehicle systems have been developed to accurately record atmospheric turbulence and other meteorological data [22–27]. These newly implemented platforms are ideal for measuring this atmospheric data. By flying through the flow, the reliance on Taylor's hypothesis is reduced. These systems are also capable of flying at essentially any desired altitude. Another major feature of these systems is their portability. Since the aircraft are generally small in size, they can be easily transported anywhere that is of interest to the user and they require very little

infrastructure for operation. While these systems are being used to make significant contributions to our knowledge of the atmospheric boundary layer, there is still one main limiting factor. Most of the vehicles employed for this type of research have relatively small payload capacities when compared to typical laboratory equipment. This issue has forced researchers to make compromises on the type of sensors implemented in the unmanned aerial vehicles.

Historically the hot-wire anemometer has been the benchmark for turbulence research in a lab setting [28]. hot-wire sensors are ideal for turbulence research due to their fast time response and high sensitivity. However, commercial systems generally require heavy desktop controllers and signal conditioners for operation. In addition, single-sensor hot-wire probes are incapable of resolving the direction of the flow.

The standard sensor used for turbulence research on small unmanned aerial vehicles has been the multi-hole pressure probe [29]. With this type of sensor, the direction of the wind can be resolved, but only a small portion of the atmospheric turbulent scales, as the time response of these sensors is more than 100 times slower than that of the hot-wire anemometer. Therefore, with a multi-hole probe it is not possible to directly measure the full spectra of turbulence down to the dissipative range. Hence the dissipation rate of the turbulence, a key descriptor of the rate of exchange of turbulent kinetic energy within the turbulence, must be inferred indirectly.

The work presented in this thesis addresses these limitations by developing an unmanned aerial vehicle system with both a portable hot-wire anemometer and multi-hole probe as part of its sensor suite. This was enabled through implementing a smaller and lighter hot-wire anemometer system on an airframe with an appropriate payload capacity. The newly developed hot-wire anemometer system completed multiple successful test flights and was demonstrated to be capable of directly measuring the full inertial subrange of the atmospheric turbulence, allowing for direct calculation of the turbulence dissipation rate.

4

Chapter 2 Background

2.1 Turbulence Theory

Turbulent flows have been an area of interest to scientist for centuries. However, the study of turbulence as we know it today did not begin until the late 19th century when Osborne Reynolds published his research on turbulent pipe flows. From these pipe flow experiments Reynolds concluded that the flow inside the pipe only became turbulent, once a certain dimensionless parameter based on the flow properties reached a certain critical value [3]. This parameter is what is known today as the Reynolds number

$$Re = \frac{\rho U L}{\mu}.$$ (2.1)

The Reynolds number is the ratio of the fluid's density, ρ, and appropriately selected velocity and length scales U and L to the dynamic viscosity μ. For example, in the pipe flow being studied by Reynolds U would be equal to the mean velocity through the pipe while L would be the pipe diameter.

The governing equations of motion for incompressible, isothermal, fluid flow are the Navier-Stokes equation

$$\rho \left[\frac{\partial u_i}{\partial t} + u_j \frac{\partial u_i}{\partial x_j} \right] = -\frac{\partial p}{\partial x_i} + \rho g_i + \frac{\partial}{\partial x_j} \left[\mu \frac{\partial u_i}{\partial x_j} \right]$$ (2.2)

describing the linear momentum balance and the continuity equation

$$\frac{\partial u_i}{\partial x_i}$$ (2.3)

describing conservation of mass. Here, for compactness, summation notation is used so that subscripts indicate Cartesian components, e.g. $i = 1, 2, 3$ with $1, 2, 3$ typically representing x, y, z. Hence, $[u_1, u_2, u_3]$ are the components of the velocity vector $\vec{u}$ aligned with the x, y and z directions respectively. Similarly, the spatial direction is given by the direction vector components x_i. Additionally, within Equation 2.2, time is represented by t, pressure by p and the dynamic viscosity of the fluid by μ. Finally, the term f_i represents conservative body forces acting on the fluid, which is usually limited to gravitational force such as $f_i = g_i$, where g_i are the components of the gravitational acceleration vector.

If one non-dimensionalizes the terms in Equation 2.2 such that $x_i^* = x_i/L$, etc., Equation 2.2, for steady flows with negligible gravitational effects, can be rewritten as

$$u_j^* \frac{\partial u_i^*}{\partial x_j^*} + \frac{\partial p^*}{\partial x^* i} = \frac{1}{Re} \frac{\partial}{\partial x_j^*} \left[\frac{\partial u_i^*}{\partial x_j^*} \right] \tag{2.4}$$

which illustrates how the Reynolds number acts as a controlling parameter describing the ratio between the inertial forces on the left hand side of Equation 2.4 and the viscous forces on the right hand side of Equation 2.4.

During his pipe flow experiments Reynolds realized the complexity of analyzing the raw turbulence data he was collecting. This inspired Reynolds to develop a statistical approach to analyze the complicated fluctuations he was observing. He accomplished this through Reynolds decomposition, splitting the time-varying variables into two parts, a mean component and a fluctuating component.

$$\Phi(t) = \overline{\Phi} + \Phi'(t) \tag{2.5}$$

where $\Phi(t)$ represents any time dependent property of the turbulent flow, and $\overline{\Phi}$ and $\Phi'(t)$ correspond respectively to the time averaged and fluctuating components of the raw signal. By substituting $u_i = \overline{u_i} + u_i'(t)$ into Equation 2.2 the incompressible

Reynolds Averaged Navier Stokes (RANS) equation can be derived as

$$\rho \left[\frac{\partial \overline{u_i}}{\partial t} + \overline{u_j} \frac{\partial \overline{u_i}}{\partial x_j} \right] = -\frac{\partial \overline{p}}{\partial x_i} + \frac{\partial}{\partial x_j} \left[\mu \frac{\partial \overline{u_i}}{\partial x_j} - \rho \, \overline{u_i' u_j'} \right]. \tag{2.6}$$

Comparison between Equations 2.2 and 2.6 shows their equivalency for the terms representing the mean flow. However due to the implementation of Reynolds averaging technique we have now introduced the Reynolds Stress Tensor, $\rho \, \overline{u_i' u_j'}$, on the right side of the equation.

The components of the Reynolds stress tensor therefore represent the influence of the turbulence on the mean flow, and are commonly key parameters used to describe turbulence. However, the approach used by Reynolds has a critical problem in that solution of Equation 2.6 is not possible due to the introduction of the new unknowns $\rho \, \overline{u_i' u_j'}$, and any attempt to derive governing equations for these unknowns using conservation of mass, momentum and energy just introduces even higher order unknown terms. This is referred to as the 'closure problem' and results in the need for empirical, or semi-empirical, modeling approaches to solve Equation 2.6. To date, no satisfactory models have been found that are universally applicable.

While Reynolds laid the ground work and developed many of the modern methods for studying turbulence, G.I Taylor took the statistical analysis of this type of data one step further and formalized several methods still used today. In the 1930's, Taylor introduced the concept of homogeneous isotropic turbulence [12] (in which the normal components of the Reynolds stress tensor ($i = j$) are identical, and all other components, ($i \neq j$) are zero). Homogeneous turbulence simplifies that problem analytically, but in general turbulence is not isotropic. However, Kolmogorov [5], working with the established concept that the kinetic energy of turbulence cascades from the large scales to the smaller scales, assumed that the 'memory' of the turbulence would be lost during this process and that the very small scales would indeed

be isotropic. This simplification made much of the work towards defining the fine structure of turbulence possible.

Another contribution made by Taylor, utilized extensively in the study of turbulence, is the 'frozen flow hypothesis' [12]. The frozen flow hypothesis states that if the mean velocity of the flow is much greater than the turbulent velocity, then it may be assumed that the changes in velocity at a single observation point are simply due to the passing of an unchanging or frozen flow pattern over that point. This hypothesis allows for a time varying signal to be transformed into a spatially dependent signal. This hypothesis is used extensively in turbulence research, as most sensors have high temporal resolution but most theory is established in the spatial domain.

2.2 Turbulence Energy Spectrum

Due to the scale dependence of turbulence, a key feature used to describe the turbulence is its energy spectrum. The energy spectrum describes how the turbulent kinetic energy

$$k = \frac{1}{2}u_i u_i \tag{2.7}$$

of the turbulence is distributed among the different wavelengths, λ (or scales) of turbulence. Typically described in wavenumber space where κ is the wavenumber defined as $\kappa = 2\pi/\lambda$, the energy spectrum of turbulence, $E(\kappa)$ is related to k through

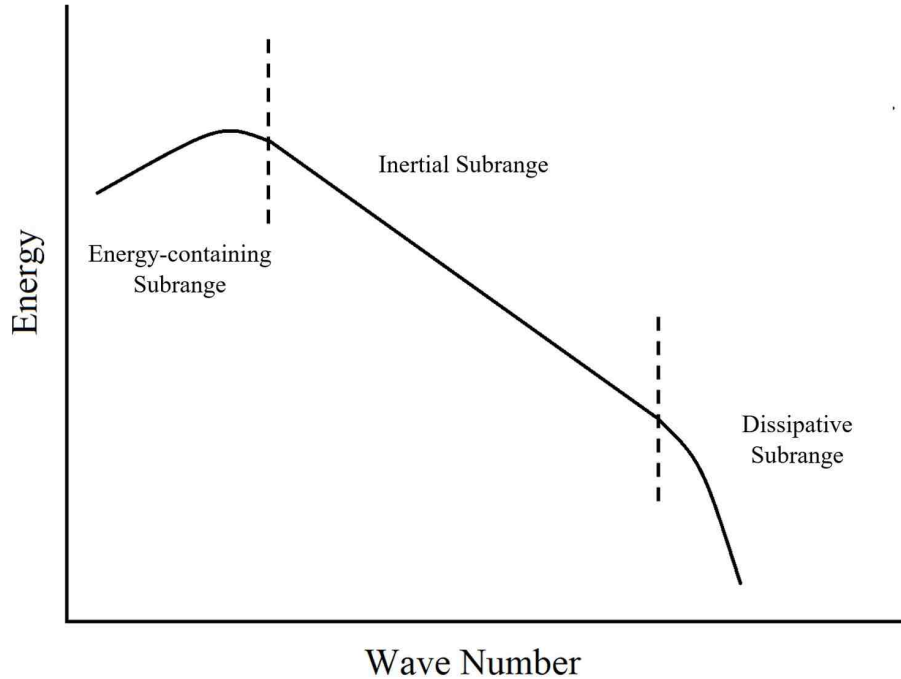$$k = \int_0^{+\infty} E(\kappa)d\kappa. \tag{2.8}$$

Figure 2.1: General form of the turbulent kinetic energy spectrum at various.

An example of turbulence energy spectrum in wavenumber space is presented in Figure 2.1. The energy spectrum is divided into three different ranges. The low wavenumber (i.e. long wavelength) portion of the spectrum describes the large-scale turbulent eddies and generally referred to as the energy-containing subrange. Kinetic energy 'extracted' from the mean flow forms energetic turbulent motions with scales on the order of L, typically the largest scales within a turbulent flow. These eddies tend to decay very slowly.

As the energy-containing eddies evolve in time, they break down into smaller, weaker eddies, redistributing their kinetic energy through what is referred to as the energy cascade [30]. This process occurs at scales too large to be impacted by viscosity, and hence this is also referred to as the inertial subrange.

Once the eddies have broken down into sufficiently small, sufficiently weak eddies they are subject to the influence of viscosity, which acts like friction to redistribute the kinetic energy into thermal energy. Thus, the high wavenumber, small wavelength,

end of the spectrum is referred to as the dissipative subrange.

The separation between the largest and smallest scales is then described by the ratio of inertial to viscous effects, which is represented by the Reynolds number. Hence, at low Reynolds number the energy containing and dissipative subranges can overlap, and an inertial subrange will only appear at high Reynolds number.

This idea of the energy cascade in turbulence was introduced in the 1920's, by a meteorologist named Lewis Richardson. Richardson was one of the first to theorize that turbulence consisted of different sized eddies which played different roles in the dissipation of energy throughout the flow.

However, it was the work of Kolmogorov in the 1940's [5], working with the assumptions of the existence of an inertial cascade and isotropy of small scales, which provided the next major advance in turbulence understanding. Kolmogorov hypothesized that at sufficiently high Re for the small-scale turbulent motions to be independent of the inertial motions, the properties of the dissipation range would be dependent only upon the mean rate of turbulent kinetic energy dissipation per unit mass, $\langle \epsilon \rangle$ and the kinematic viscosity of the fluid, $\nu = \mu/\rho$.

These concepts allowed Kolmogorov to use scaling arguments to define the Kolmogorov scales

$$\eta = \left(\frac{\nu^3}{\langle \epsilon \rangle} \right)^{\frac{1}{4}} \tag{2.9}$$

$$v_K = (\nu \langle \epsilon \rangle)^{\frac{1}{4}} \tag{2.10}$$

$$\tau_K = \left(\frac{\nu}{\langle \epsilon \rangle} \right)^{\frac{1}{4}}, \tag{2.11}$$

which describe the smallest length (η), velocity (v_K), and time (τ_K) scales of the turbulence which could contain any measurable amount of k. Therefore the high wavenumber range of the spectrum will scale with these terms, and for $\kappa > 2\pi/\eta$ the energy content of the turbulence approaches zero.

Kolmogorov's second hypothesis addresses the inertial subrange. Assuming that the Reynolds number is sufficiently large that there is no overlap between the energy containing and dissipative eddies, Kolmogorov hypothesized that there would be a range of scales where the turbulent scales were too small to be adding energy from the mean flow, and too large to be losing energy to viscosity. Hence the eddies within this region would also be isotropic, with a rate of transfer of kinetic energy depending only on $\langle \epsilon \rangle$. Scaling arguments were then used to derive what is now referred to as the 'minus five-thirds law', which states that within the inertial subrange

$$E(\kappa) \propto \langle \epsilon \rangle^{\frac{2}{3}} \kappa^{-\frac{5}{3}}. \tag{2.12}$$

This is illustrated on the logarithmic axes of Figure 2.1 by a region with constant slope.

The energy containing eddies on the other hand have no theory defining their general shape since the turbulence at these scales depend almost exclusively on the external conditions of the flow. These are the scales in which turbulent kinetic energy is introduced into the flow through external forces such as mean shear or buoyant production. If k production were halted these eddies would decay at a rate proportional to $\langle \epsilon \rangle$. Since the turbulent production occurs in this range of scales, the peak of the turbulent energy spectrum will occur inside this range.

Kolmogorov's hypotheses are the foundation of many models for small-scale turbulence, despite the early recognition that $\langle \epsilon \rangle$ was an imperfect descriptor for the dissipation rate. This imperfection arises from the observation that $\epsilon(x_i)$ is not evenly distributed in space, and is instead concentrated in highly localized regions of intense dissipation, referred to as internal intermittency. Hence, the distribution of ϵ is highly skewed, and the mean quantity $\langle \epsilon \rangle$ does not represent these properties. Many attempts have been made to address this deficiency [31], including by

Kolmogorov [32]. No suitable theory has yet to satisfactorily capture the effects of internal intermittency. However, the effects of internal intermittency are largely limited to higher order effects, and Kolmogorov's theories have formed the backbone of modern turbuelence theory.

Chapter 3 Motivation

A complete statistical description of the small-scale turbulence remains elusive, complicated by the lack of suitable experimental results which can be used to validate these theories. There are two aspects to this problem. The first is that the turbulence must be at sufficiently high Reynolds numbers for an inertial subrange to exist. This is a challenging prospect, given that for most laboratory facilities (wind or water tunnels), achieving high Reynolds numbers requires increasing U and L to very high values. The need to keep the flow incompressible limits U, so L must be quite large. Although some pioneering work has been conducted in large-scale NASA facilities [33], most existing high Reynolds number facilities increase the Reynolds number by decreasing ν. However, these facilities are relatively rare [34] and introduce their own diagnostic challenges [7, 35, 36].

The second challenge to address is that the energy content of the turbulence is described in wavenumber space. However most sensors, particularly those used in high Reynolds number turbulence, measure in time, rather than space. This introduces a significant challenge as the advection velocity of turbulence can be wavenumber dependent, whereas Taylor's frozen flow hypothesis assumes a constant adcvection velocity. This can potentially bias observations of wavenumber dependence, when acquired with temporal sensors [14].

The approach taken here to address these challenges is to use the atmospheric boundary layer as the turbulence producing flow which, due to the length scales involved, naturally produces high Reynolds number turbulence. To address the chal-

lenge imposed by limitations due to Taylor's frozen flow hypothesis, the objective is to measure the turbulence using unmanned aerial vehicles. At sufficiently high aircraft velocity, the wavenumber dependence of the advection velocity is mitigated and the measurements closely approach that of spatial, rather then temporal, sampling. This then is the origin of the Boundary Layer Unmanned Experiments Categorizing Atmospheric Turbulence (BLUECAT) project, in which atmospheric boundary layer turbulence is sampled using unmanned aerial vehicles.

Chapter 4 Previous Airframe Development

The BLUECAT project, beginning in 2012, has seen much development over the last seven years. Ths project was initiated, as a proof of concept aircraft, BLUE-CAT 0. BLUECAT 0 was a commercial-off-the-shelf, almost ready to fly (ARF) Senior Telemaster kit. This plane was assembled and then instrumented with a single hot-wire anemometer mounted on the leading edge of the wing. The data from the BLUECAT 0 flights proved that measurements using hot-wire probes could be successfully conducted using a small unmanned aerial vehicle (UAV).

4.1 Early Airframe Development

The early airframes in the BLUECAT project saw significant changes from their predecessor BLUECAT 0. BLUECATs 1 and 2 were custom UAVs specifically designed to carry heavy and bulky hot-wire anemometry systems and the corresponding data acquisition systems required to log the necessary high data rates. These aircraft were designed and built by students in the University of Kentucky's Unmanned Aerial Vehicle Laboratory.

Figure 4.1: BLUECAT 1 airframe designed and built in house at the UK Unmanned Systems Lab.

Both of these platforms were large carbon fiber airframes, with pusher propeller configuration to allow implementation of the instrumentation through the nose of the aircraft, and powered by gasoline engines in order to minimize electrical interference from the propulsion system and provide high endurance. While this configuration was desired for carrying the instrumentation systems, it was found that the cost and time required to manufacture and maintain these systems was very high. Both of these systems did see some level of success, but struggled to perform reliably due to issues with the gasoline motors, resulting in their retirement from the program before conducting any measurements using the systems they were designed to carry.

Figure 4.2: BLUECAT 2 airframe designed and built in house at the UK Unmanned Systems Lab

4.2 BLUECAT 3 and 4

In order to limit the amount of time that was being used in airframe design and manufacturing, BLUECAT 3 and 4 were selected to be built around commercially available airframes that could be customized to carry the instrumentation packages. Implementing these commercially available airframes provided a significant reduction in construction and repair time, at a fraction of the cost of the previous systems.

The BLUECAT 3 airframe was developed from the ARF Super Falcon 120 kit. This airframe, originally intended to be powered by a model jet turbine engine, was adapted to use a standard gasoline propeller motor. The Super Falcon 120 was also a pusher configuration, preserving some of the design advantages of BLUECAT 1 and 2. However, the major limitations of this airframe were fuselage space and the

unreliable gasoline power system. The usable fuselage was only 14 cm at the widest point, this made it extremely difficult for the researchers to have any access to the instruments at the field, and compromises had to be made to allow for the hot-wire system to be implemented. Although some successful hot-wire anemometry flights were conducted, vibration of the probe mount introduced by the reciprocating engine was found to damage probes at a high rate, resulting in retirement of the aircraft from the program.

Figure 4.3: BLUECAT 3 airframe equipped with hot-wire instrumentation.

The BLUECAT 4 airframe was the commercially available DJI S1000 octacopter. This airframe was the first rotorcraft to be used in the BLUECAT project and was selected due to its payload capacity. However, BLUECAT 4 had to be customized to incorporate the instrumentation. To house the DAQ and other larger instruments, a tray system was suspended beneath the main body. Since the hot-wire anemometer had to be mounted outside of the downwash of the propellers, a large cantilevered boom was secured to the airframe allowing the hot-wire sensor to be extended out beyond the disturbances caused by the rotorcraft in flight. This airframe offered much

better space and accessibility to the instrumentation. However the flight endurance was very short (10 min) due to the heavy payload. More importantly, the signal to noise ratio of the hot-wire was very low, due to the large number of electric motors, and the reduced sensitivity of the hot-wire at low cooling velocities. This airframe was repurposed to carry different instrumentation, and the use of the hot-wire system as the primary turbulence sensor put on hold.

Figure 4.4: BLUECAT 4 multi-rotor equipped with hot-wire instrumentation.

4.3 BLUECAT 5

Based on the accumulated experience from BLUECAT 0 through 4, BLUECAT 5 was based on the Skywalker X8 platform. This was a large foam flying wing with a spacious payload bay that offered plenty of space and accessibility to all of the instrumentation. BLUECAT 5 was the first fixed-wing BLUECAT airframe to use an electric propulsion system. The increased reliability of the electric system was the largest benefit of this airframe over the previous airframes. BLUECAT 5 was also the first system to not incorporate a landing gear, instead it was launched buy a small bungee launcher and used a belly skid landing technique. This feature of the airframe removed the need for a paved runway, thus opening the door to flying in

more remote locations that may be of interest to the researchers. Another first for this airframe was the use of a five-hole probe (FHP) in place of the hot-wire anemometer. The FHP increased reliability of the sensor package due to its increased durability over the extremely fragile hot-wire anemometer. Unlike the hot-wire probe, the FHP was also able to provide wind direction, as wall as velocity. Another advantage was the decreased payload requirement, since the circuitry driving the FHP was only a fraction of the size and weight of the hot-wire system. The drop in payload size in turn caused an increase in flight duration, that allowed the BLUECAT 5 airframe to fly up to one hour on a single battery. BLUECAT 5 proved to be a very successful airframe completing hundreds of successful flight experiments [23, 37].

While the use of a FHP was key to the success of this airframe it was also the biggest drawback. FHP sensors, by nature, have relatively low frequency response and spatial resolution. The response of the FHP was only $\mathcal{O}(10)$ Hz, compared to that of a hot-wire at $\mathcal{O}(10)$ kHz. As a result, the spatial resolution becomes of the order of $\mathcal{O}(1)$ m, as apposed to being of the order of $\mathcal{O}(1)$ mm. Note that the Kolmogorov scale in the atmospheric boundary layer is $\mathcal{O}(1)$ mm. Hence, this change in instrumentation prevented full resolution of the atmospheric turbulence.

Figure 4.5: BLUECAT 5 equipped with five hole probe instrumentation.

4.4 BLUECAT 6

The desire to maximize resolution of the atmospheric turbulence led the development of the BLUECAT 6 airframe, designed and built from scratch by a group of University of Kentucky undergraduate students led by the author. The goal of this airframe was to create a larger, more durable, and more customized version of the BLUECAT 5 system, and one capable of utilizing hot-wire probes. BLUECAT 6 was a large carbon fiber flying wing airframe with a wingspan of just under 10 ft, and impressive fuselage space and accessibility.

Figure 4.6: BLUECAT 6 prepared for takeoff on its maiden flight.

One major advantage of this airframe was the use of a pallet system that allowed the entire instrumentation system to be removed from the plane for bench testing or maintenance. The large airframe proved to be very efficient, with one 28,000 mAh

battery pack the flight endurance was approximately 2 hours. BLUECAT 6 had an empty weight of 18 lbs (including battery), this meant the airframe had an available payload weight of approximately 5 lbs.

The primary goal of the BLUECAT 6 airframe, was to re-introduce the hot-wire anemometer back into the instrumentation system, since it had been removed as payload for the smaller BLUECAT 5 airframe. BLUECAT 6 had a handful of successful flights, however, the airframe showed signs of stability issues, which eventually led to the loss of the airframe. Again due to the cost and time it takes to build and repair these type of systems, a commercially available option was selected to fill the role of BLUECAT 6.

4.5   Comparison of BLUECAT Airframes

Two key quantifiable attributes of the BLUECAT airframes are the flight endurance and the frequency response of the sensor suite. An ideal system would maximize both of these parameters. (Figure 4.7) provides a good visual of the differences between each of the previous BLUECAT airframes as well as the current BLUECAT 6B airframe.
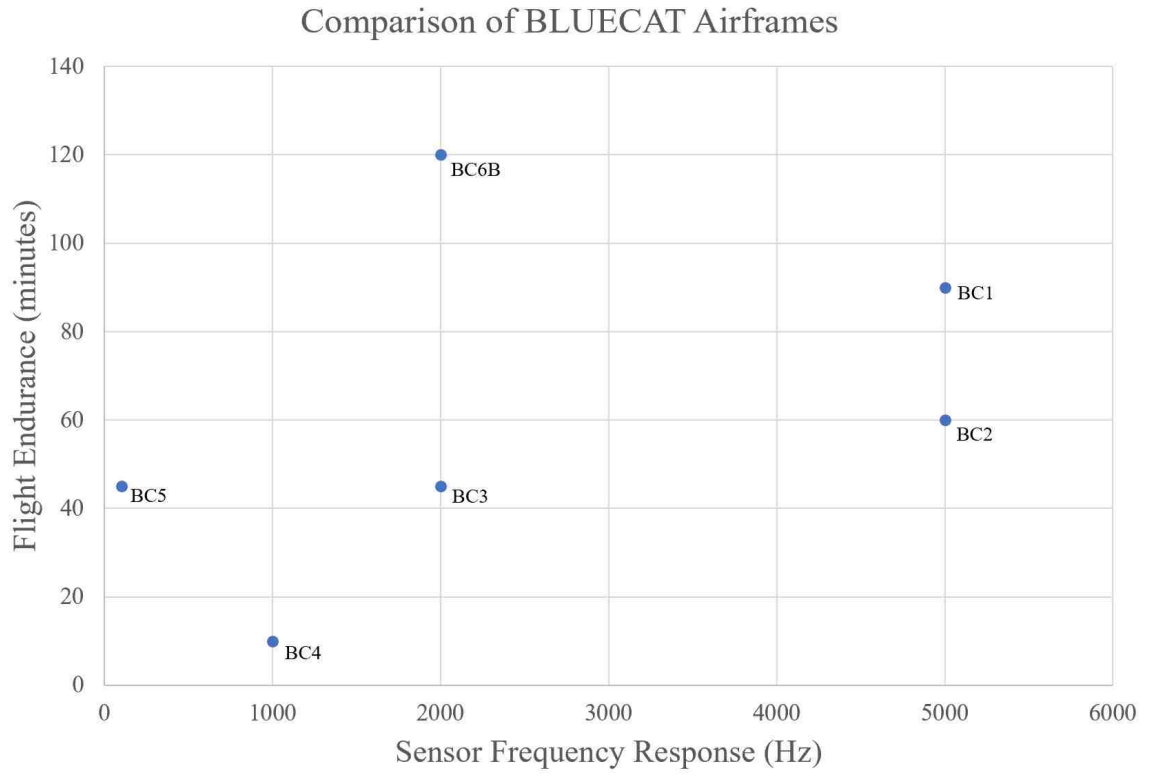
Figure 4.7: Comparison of BLUECAT airframe capabilities.

Chapter 5   Current System Development

Until the BLUECAT 5 airframe the hot-wire anemometor was the intended sensor for measuring the fluctuating component of velocity, u'_1, where 1 indicates the component of velocity parallel to the probe axis. This type of sensor is used extensively in laboratory studies of turbulence due to its sensitivity and time response. When employed in a laboratory environment, these characteristics allow the researcher to observe the smallest scales of the turbulence when using Taylor's frozen flow hypothesis.

As noted in the previous chapter, the hot-wire instrumentation was not implemented in the BLUECAT 5 airframe, and a multi-hole probe used instead. This wind sensor, while lacking in sensitivity and time response, offered some advantages with its durability, lightened payload, and ability to capture both wind speed and direction.

Thus, the objective of the BLUECAT 6 aircraft was to develop an aircraft capable of operating both types of sensors. The combination of the two sensors provides the ability to calibrate the hot-wire probe in situ and resolve three components of velocity using the FHP, while introducing the capability two measure one component of velocity with two orders of magnitude finer resolution with the hot-wire probe. In addition to wind speed and direction, BLUECAT 6 was also designed to measure pressure, temperature and humidity, alongside the aircraft's position and orientation. The combination of these variables allow the researcher to characterize the turbulence within the atmospheric surface layer in detail.

5.1 BLUECAT 6B Airframe

With the loss of the BLUECAT 6 aircraft, the decision was made to find a commercial off the shelf airframe capable of meeting the same capabilities as provided by the BLUECAT 6 aircraft. Referred to as the BLUECAT 6B airframe (Figure 5.1), the aircraft is built around the Believer long-range aerial mapping and surveying aircraft. Long range and high payloads for this aircraft are accomplished through its aerodynamic design and the use of a twin tractor power system. This setup gives the airframe the ability to have enough thrust to takeoff and fly with extremely heavy payloads while drawing minimal power from the battery during cruise. The Believer is constructed of lightweight EPO foam and has a wingspan of 1960 mm. Overall this is a very well designed airplane that is convenient to work with and performs consistently in the air.

Figure 5.1: BLUECAT 6B otufitted with hot-wire anemometer and five hole probe sensors.

The batteries selected to power this airframe include a Titan Power 6S 28,000 mAh LiIon battery pack, which provides power to the electric motor propulsion and all on board instruments apart from the hot-wire anemometer. The electric propulsion system consists of two counter rotating KDE3510XF-475 (475kv) brushless motors turning $12" \times 12"$ APC props, the speed controllers driving the motors are Hobbywing XRotor 40A. The flight control surfaces were reinforced with a heat activated laminant and are driven by high speed metal gear servos. The airframe is also equipped with a Pixhawk autopilot that allows for autonomous flight following a planned flight path. The fuselage space and accessibility is adequate, while the carrying capacity is exceptional. BLUECAT 6B has a fully loaded weight of 13.5 lbs, even at this weight the airframe handles takeoff and landing with ease and cruises at 22 m/s for

approximately two hours.

5.2 BLUECAT 6B Instrumentation

The main goal of the BLUECAT 6B airframe is to capture the turbulence in the atmospheric surface layer flow. To do this the airframe uses a multi-hole probe along with a hot-wire anemometer to record wind speed and direction. A VectorNav 300 navigation system is used to provide accurate position and orientation of the aircraft. An iMet XQ-UAV sensor supplements this data with pressure temperature and humidity, giving the ability to calculate air density.
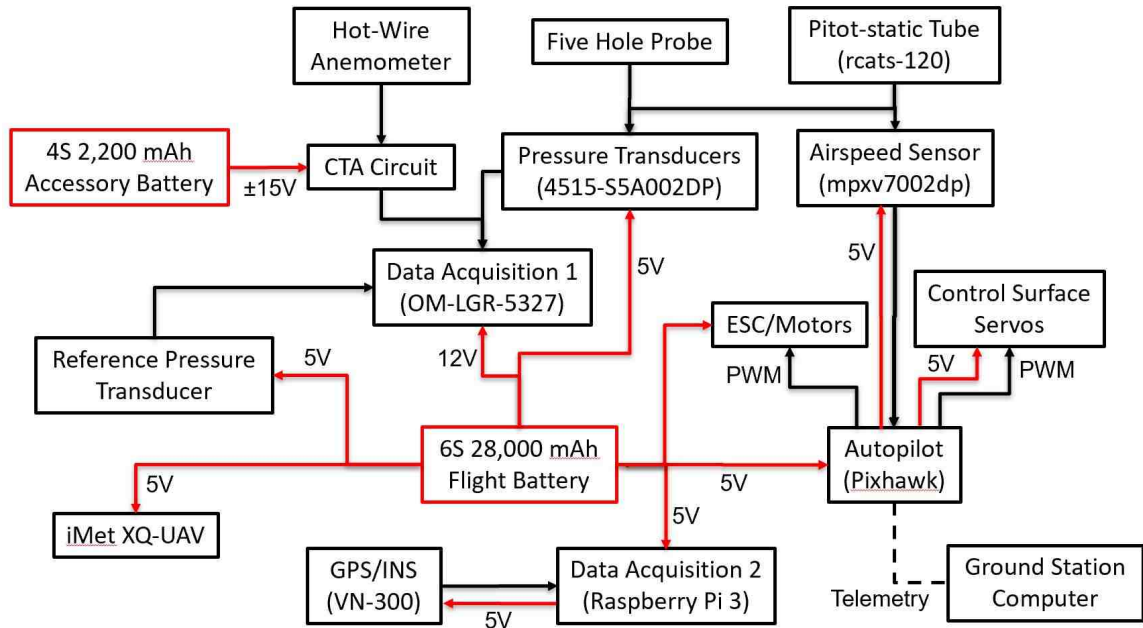
Figure 5.2: Block diagram of BLUECAT 6B instrumentation system.

5.2.1 Hot-wire Anemometer

The primary instrument on board BLUECAT 6B is the hot-wire anemometer. A hot-wire anemometer is a device used to measure the speed of a fluid flow, by taking advantage of the relation between the flow speed and the convective cooling coefficient [28,38]. In general a hot-wire probe is made up of two small needles with an extremely

27

thin wire suspended between them, the probe on BLUECAT 6B used a wire diameter of 2.5 microns. This probe, which has a known resistance, is then inserted into one branch of a Wheatstone bridge circuit. Allowing the circuit to modify the amount of electrical current being sent to the probe based on the probes resistance at that moment in time. More specifically, the hot-wire anemometer used by BLUECAT 6B is a constant temperature anemometer (CTA), which means the circuit works to keep the wire's temperature constant by increasing or decreasing the amount of current passing through the wire. This is accomplished using the relation between the resistance of the wire and its temperature. In general, the sensor relies on the change in flow speed to cool the wire which, in turn, decreases the wire's resistance. To compensate for this change in resistance the driving circuit delivers more current to the probe which heats the probe back to the constant temperature/resistance required to balance the Wheatstone bridge. Conversely, if the flow speed decreases, the wire increases in temperature and resistance and the imbalance of the Wheatstone bridge causes a reducing in current provided to the wire. By measuring the current provided to the wire, and utilizing a calibration of this measured current as a function of cooling velocity, one can find the fluid flow velocity .

The hot-wire anemometer is an extremely sensitive device that is vulnerable to electric noise. In order to minimize the effect of the electrical noise the circuit is powered by an isolated power source through a linear voltage regulator. Power for the hot-wire anemometer is pulled form a separate 4S 2,200 mAh LiPo pack. Shielding was also put in place to further reduce electromagnetic interference in the signal. All cables in the system are shielded BNC cables and additional shielding was added to protect the sensitive circuit from the high-noise cabling that provides power to the electric motors.

The CTA circuit in BLUECAT 6B is a modernized, and portable version of the Melbourne University Constant Temperature Anemometer (MUCTA) circuit [39],

custom made for this application as part of a prior student's work (Figure 5.3). This custom printed circuit board is much smaller and lighter than any other commercially available CTA circuit and features a Wheatstone bridge with a 10:1 bridge ratio and an adjustable decade resistor for balancing, allowing the user to modify the circuit to be used with probes whose resistance may vary significantly. All flight experiments were conducted using an overheat ratio (the ratio of the wire temperature when hot to when cold) of 1.8, implemented using the decade resistor set to a value $180\times$ the resistance of the wire when cold, after correcting for the lead resistance.
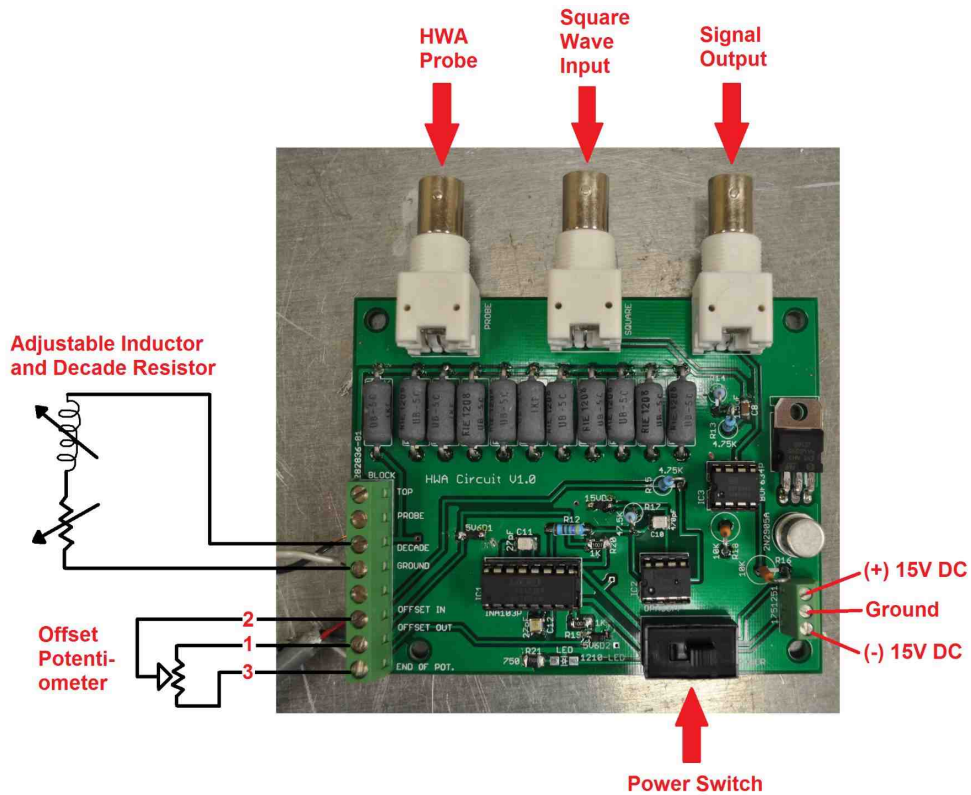
Figure 5.3: Constant temperature anemometer control circuit.

Due to the f^2 feedback noise inherent to CTA systems [40], a critical consideration when conducting hot-wire measurements is the use of a low-pass bias filter to conditioning the output signal prior to digitization. For this purpose BLUECAT 6B uses a Thor Labs passive 5th order Butterworth low-pass filter. This filter has a cutoff

frequency of 10 kHz.

The hot-wire probes used on the BLUECAT 6B airframe were manufactured from 2.5 micron diameter Pt Wollaston wire soldered by hand to a TSI Model 1201 Disposable Probe body. Once soldered the wires were then etched by applying a 15% dilluted nitric acid/water solution to a section of the wire, and then exciting the solution with a small electric current. The etching process exposed a 500 micron length of the platinum wire core, which acts as the sensing length with an aspect ratio of 200.

Because the hot-wire circuit is so sensitive, small variations in the physical attributes of each of the probes can cause the circuit to behave differently. This means the circuit must be individually tuned for each of the probes. This ensures that the sensors response will be optimum for each probe that is installed. While the tuning process is fairly involved and is much easier to complete in a laboratory environment, all of the tools needed are small and portable so that this process could be completed at the field immediately prior to flying. This process involves using a small air compressor to create a consistent jet of air that can be adjusted to match the average cruising velocity of the UAV. Once the hot-wire probe is installed and the jet is applied, a 1 kHz square wave is inserted into the middle port of the CTA circuit. The output of the circuit is then observed using a small portable oscilloscope. By adjusting the offset potentiometer, decade resistor, and adjustable inductor you can tune the circuit until the sensor's output is optimized. Generally the sensor is tuned in order to maximize the frequency response, however the system installed in BC5B is limited at 10 kHz due to the low-pass filter. Therefore, 10 kHz will be the fastest time response that can be acheived with the current system. (Figure **??**) shows the response of the hot-wire circuit after the tuning process has been performed.
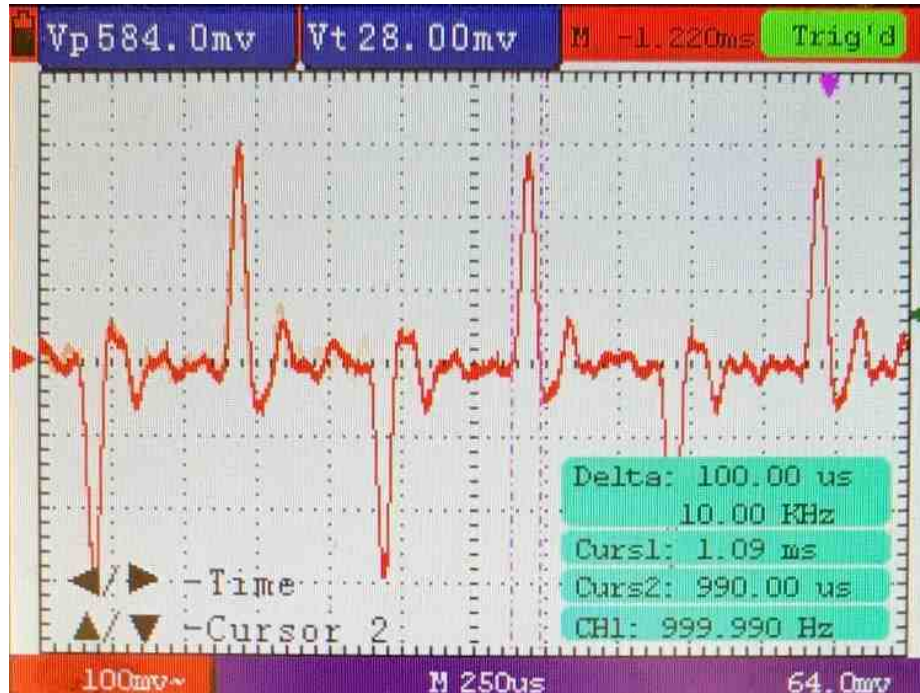
Figure 5.4: Optimized response of the hot-wire anemometer during tuning with a 1 kHz square wave input.

5.2.2 Five-Hole Probe

In addition to the hot-wire anemometer, the wind speed was also captured by the five-hole probe (FHP). A FHP is a small wind sensor with a beveled tip that has one center hole surrounded by four other holes. This sensor works by measuring the dynamic pressure at each of these holes individually and comparing them to a common static pressure. Using a detailed calibration process [23], it is possible to relate the five pressure differences to the flow speed and direction.

The major limitation of the FHP is its poor frequency response when compared to the hot-wire probe. In order to better understand the time response of these probes a few tests were performed. The first test involved using a balloon to create a constant pressure on the probe, then popping the balloon to cause a step change in the pressure seen on all five holes, the time response of the probe was then defined as the settling time of the signal. The second test implemented a speaker in an enclosed chamber

31

that could be used to generate a pressure wave at any given frequency. To test the probe's response, the frequency of the pressure wave was simply incremented until the amplitude of the signal began to be attenuated, signifying a loss of sensitivity. Both of these tests gave roughly the same results, showing that the five hole probe had time response of roughly 80 Hz.

The FHP requires directional calibration prior to flight in order to translate the pressure values into velocity magnitude and direction. This calibration was performed in a wind tunnel at The University of Kentucky using two stepper motors to position the probe at a known angle in a controlled flow velocity. The probe was positioned at pitch and yaw angles ranging from -30 to 30 degrees, then the signal from the pressure transducers was averaged over a period of two seconds. Using these known reference positions a set of calibration coefficients were derived. This process is described in much greater detail by Witte [23].

5.2.3 Navigation System

To successfully resolve the smallest scales of atmospheric turbulence, it is crucial to have an accurate position, orientation, and velocity of the airframe at all times. To accomplish this, BLUECAT 6B employed a VectorNav VN-300 Rugged, a small dual GNSS-Aided Inertial Navigation System. By implementing two GNSS antennas, the VN-300 is able to accurately sense the vehicle's heading without relying on vehicle dynamics or magnetic sensors. The VN-300 has the capability to provide the vehicle heading with an uncertainty of ± 0.3 degrees and roll and pitch at ± 0.1 degrees. Ground velocity is another extremely important measurement that is provided by the Vectornav. The VN-300 boasts a velocity accuracy of ± 0.05 m/s.

5.2.4 iMet XQ-UAV

The iMet XQ-UAV sensor is a small self-contained weather sensing unit. The iMet has built in sensors to record pressure, temperature, and humidity, as well as memory storage and an internal battery so that the sensor can be operated completely isolated from the rest of the instruments. The iMet sensor also has a built in GPS that provides the latitude, longitude, altitude, and time stamps.

5.2.5 Data Acquisition

The data acquisition for this system is completed in three locations. As previously mentioned the iMet sensor has self contained memory storage and therefore requires no external DAQ. Pressure, temperature and humidity data is logged onboard the iMet at 1 Hz.

For the hot-wire and FHP sensors, the primary DAQ for the system is an Omega OM-LGR-5327. This DAQ offers 16 analog input channels with a range of +/-30V and a 16 bit resolution. The device is also capable of very high sample rates with a maximum aggregate sample rate of 200 kS/s. Finally the DAQ features an SD card drive for internal memory storage, as well as a push button trigger event.

For the VectorNav system, the secondary data acquisition is accomplished with a Raspberry Pi 3 communicating with the VectorNav via serial data stream and storing the 6 degree of freedom kinematic information of the aircraft at a rate of 200 Hz.

5.2.6 Data Reduction

The FHP, iMet and VectorNav signals are amalgamated to provide pressure, temperature, wind speed and direction using the basic procedure previously established for BLUECAT 5 and described in Ref. [23]. However, there is one small difference in the alignment of the three separate time signals. For the BLUECAT 6B system, a separate reference pressure transducer was installed and recorded by the primary

Omega DAQ along with the FHP and hot-wire anemometer data. Previously, without the static pressure measurement, there was no way to directly align the FHP signal with the VectorNav data. Instead, the Pixhawk telemetry data was required. In the previous procedure the Pixhawk airspeed was used to align the FHP and Pixhawk data and the Pixhawk GPS velocity was used to align the Vectornav and Pixhawk data. This two step alignment process decreases the accuracy of the system by introducing the possibility of compounding errors. The current system removes this issue since all three signals are able to be directly compared using the barometric pressure as the reference signal.

The procedure established to introduce the hot-wire into this instrumentation system is described in the next chapter.

Chapter 6   Results

This chapter presents the results from a successful flight test conducted on March 1, 2019. Procedures established to calibrate the hot-wire anemometer in flight are described, and results from the flight test establishing the ability to measure the dissipation rate are introduced.

6.1   Experiment Setup

This experiment was conducted at the University of Kentucky North Farm. The farm, typically used for agricultural research, offers a large open landscape with good visibility. These characteristics make it an ideal location for flying large flight patterns while operating from a fixed ground station location.

This flight experiment required three researchers, including a visual observer/ground station monitor, a pilot, and a test lead. The visual observer was responsible for monitoring the UAV status via the ground station controls while also physically observing the aircraft in flight. The pilot manually conducted the takeoff and landing portion of the flight, and held the transmitter ready to intervene if anything were to behave unexpectedly. The test lead was responsible for handling the instrumentation before and after the flight. During the flight the test lead assisted with communication between the pilot and visual observer.

The flight under consideration consisted of a large square-shaped pattern, oriented so that the legs of the box were aligned with the cardinal directions. The flight plan programmed in the Pixhawk flight controller is shown in Figure 6.1.

Figure 6.1: Flight path shown in the MissionPlanner software.

Each leg of the square pattern had a length of approximately 1400 m. This leg length was limited by the FAA requirement to maintain visual line of sight throughout the entire flight. To satisfy this requirement and maximize the leg length it was necessary to locate the ground station in close proximity to the center of the square flight path, the location of the ground station is denoted by the green balloon in 6.1.

The ground station location is at the home position for the flight, and is therefore the reference for all positional data. The altitude at the reference location is known to be 277 m above mean sea level (MSL). The ground station consisted of one laptop computer running the Ardupilot MissionPlanner software. MissionPlanner is a full

featured ground station application for the Ardupilot open source autopilot project. This software provides operators with real time orientation and position feedback as well as other necessary control data such as airspeed, battery voltage, etc. This information is all handled on board the aircraft by the Pixhawk autopilot and then transmitted to the ground station via a 3DR 915 MHz telemetry antenna. This data transmission is extremely reliable over the distances seen during this flight, however in the event that this telemetry communication is interrupted the UAV will simply continue along its programmed flight path and will resume communication once the telemetry link is restored.

The experiment took place on March 1, 2019 ranging from approximately 1600 to 1800 Eastern Standard Time. The weather conditions during the experiment were less than ideal. The temperature during the flight was roughly 3° C, and the mean wind velocity was relatively low at approximately 4 m/s. There was a dense cloud cover and some light precipitation throughout the second half of the flight.

6.2 Instrumentation Calibration

The calibration curve for the hot-wire anemometer was found through comparison with the previously validated five hole probe. To construct valid calibration curves, both signals were filtered digitally using a 6th order low pass Butterworth filter with a cutoff frequency of 50 Hz. This was done to remove the noise associated with the hot-wire anemometers much higher frequency response with the frequency of the filter selected to correspond to the approximate frequency response of the five-hole probe. Once the signals were filtered to 50 Hz, King's law (equation 6.1) was implemented to find the relation between the hot-wire anemometer output voltage and observed flow velocity.

$$E^2 = A + BU^n \tag{6.1}$$

Where E is the hot-wire response voltage and U is the flow velocity, n is a constant that is generally assumed to equal 0.5. Substituting the five hole probe velocity magnitude for U and the hot-wire voltage output for E allows for solving for the constants A and B by simply applying a linear regression for E^2 as a function of U^n. Rearranging the previous equation the flow velocity can be defined as a function of the hot-wire voltage and the three constants.

$$U = ((E^2 - A)/B)^{1/n} \tag{6.2}$$

Applying this equation to the unfiltered hot-wire response voltage will provide the high frequency flow speed data.

Once this raw flow speed data had been obtained the next step is to subtract out the velocity of the sensor. This was accomplished using the ground speed reported by the VectorNav GPS. Negating the aircraft's ground speed from the raw flow velocity isolates the wind speed in the data set. Typically with FHP measurements we must also consider the orientation of the sensor, however since the hot-wire anemometer is only capable of providing a single component velocity, the small angular variations seen in the straight line flights can be ignored.

As the flight under consideration consisted of a box shaped flight pattern, this calibration process was conducted on each leg of the box individually to remove any bias from sensor drift, or the non-stationarity of the flow field. Results of this calibration process are detailed in Figure 6.2-Recomp4.
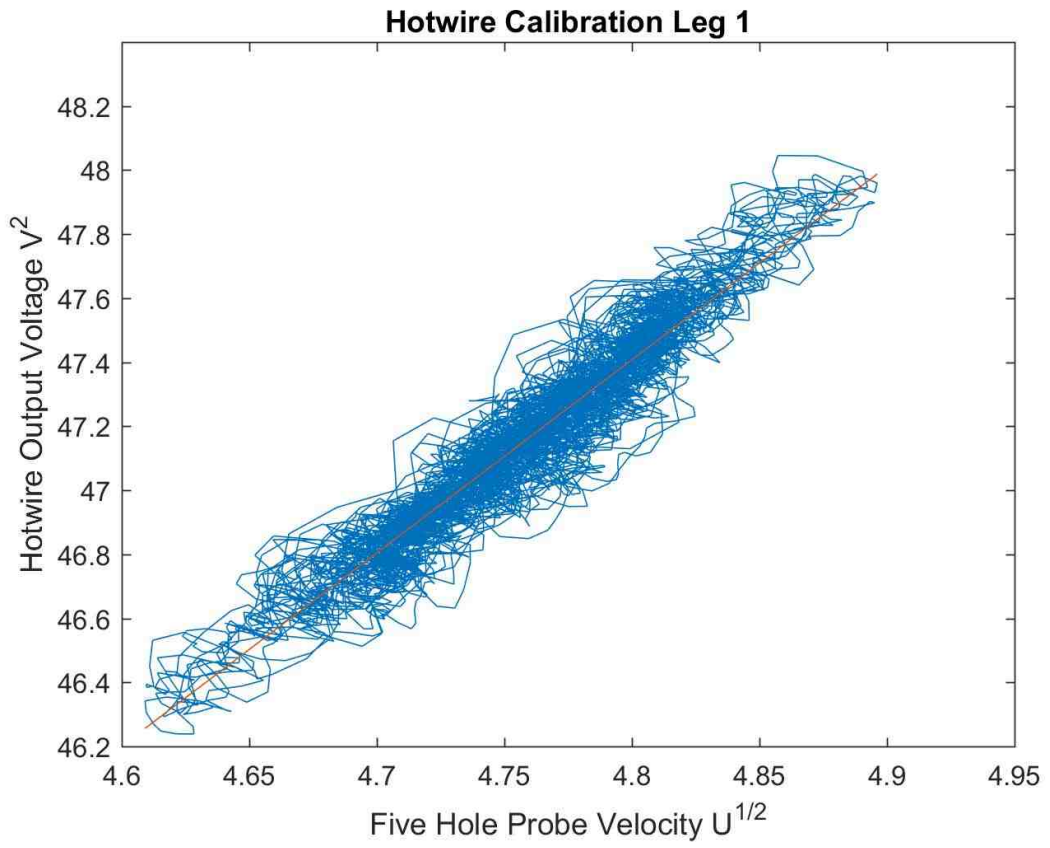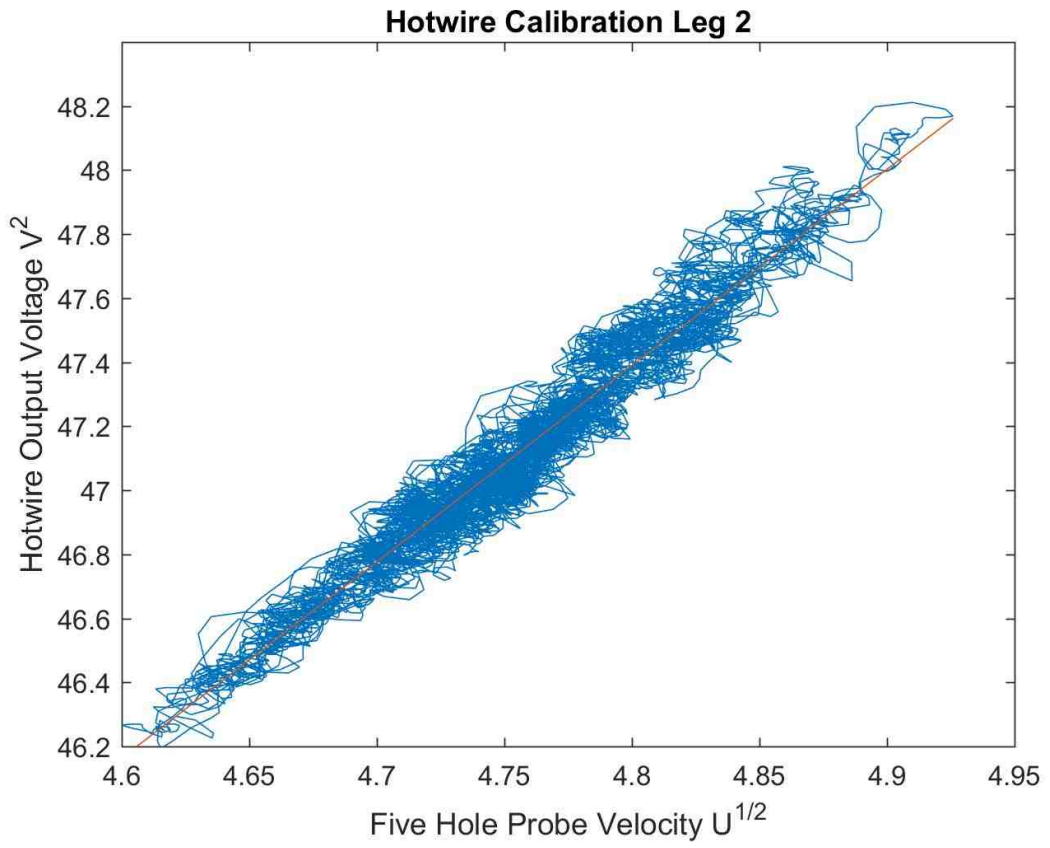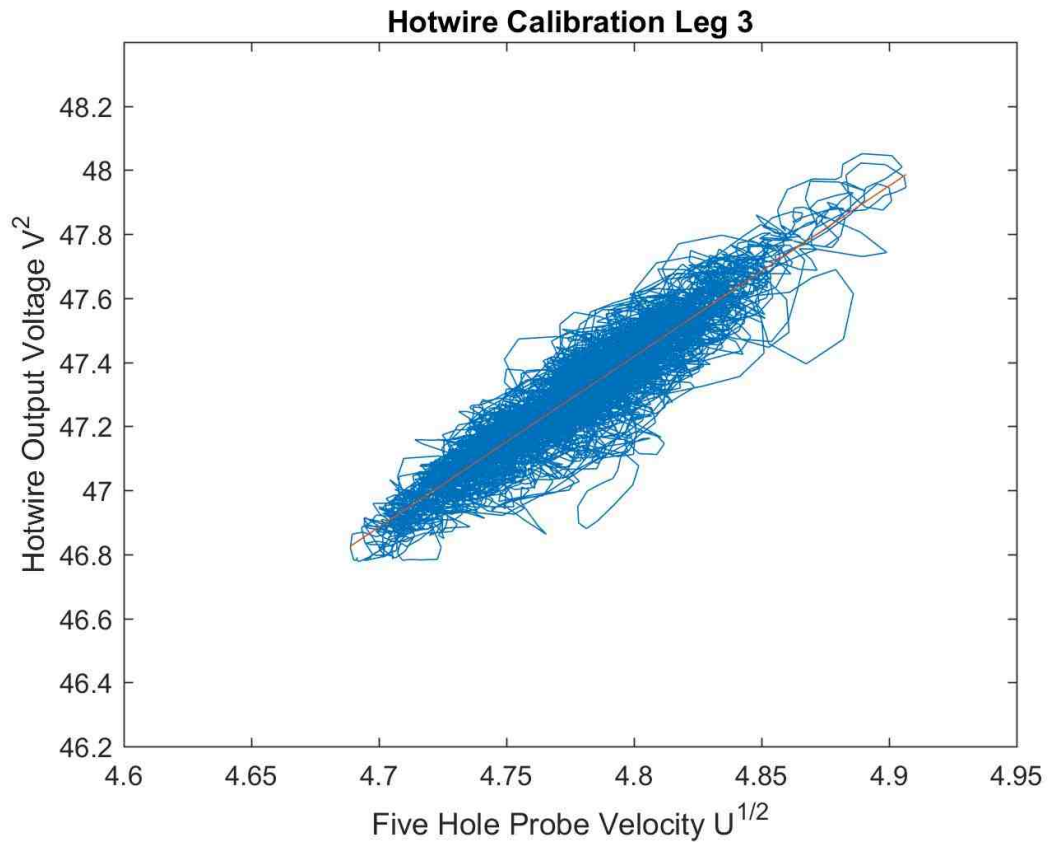
Figure 6.2: hot-wire anemometer calibration: Leg 1
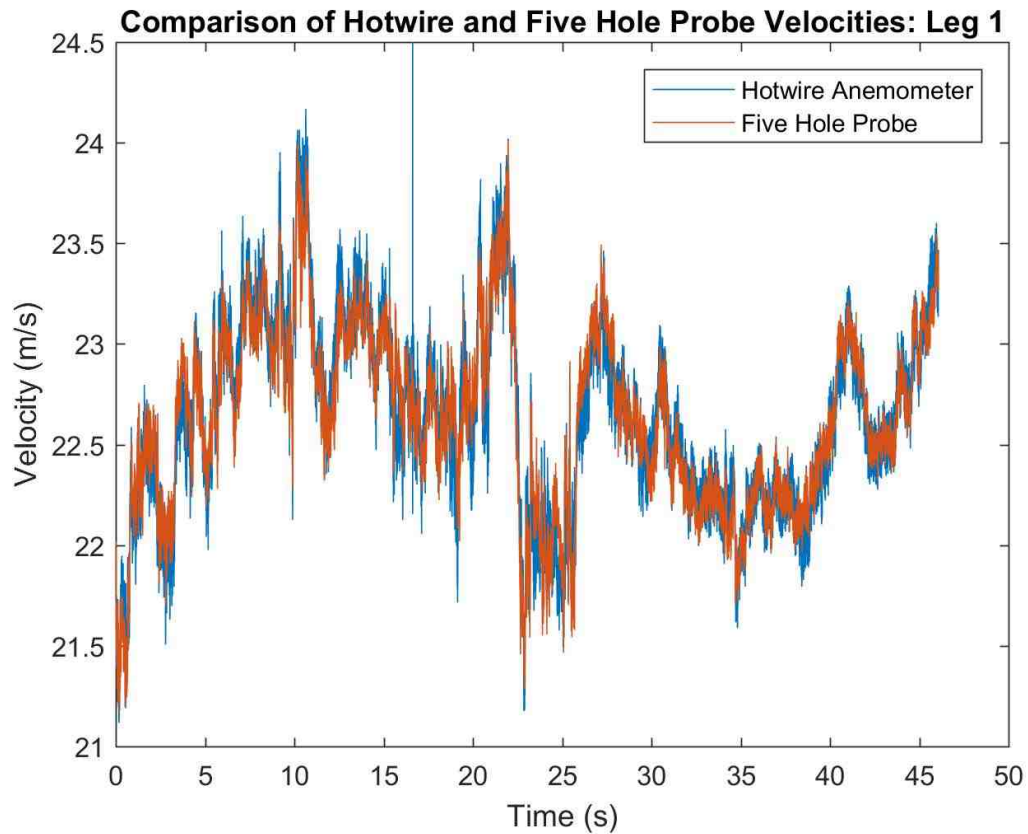
Figure 6.3: Comparison of flow speed reported by hot-wire anemometer and five hole probe

Figure 6.4 is a zoomed in view of the data presented in figure 6.3. The data presented in figure 6.4 describes a period of approximately 0.2 seconds. This plot provides a clear image of the differences in high frequency content of the two data sets. One interesting feature captured in this plot is the appearance of a characteristic resonance frequency in the oscillations of the five-hole probe signal. This resonant frequency is a result of the volume of air contained within the probe and tubing system of the five-hole probe.
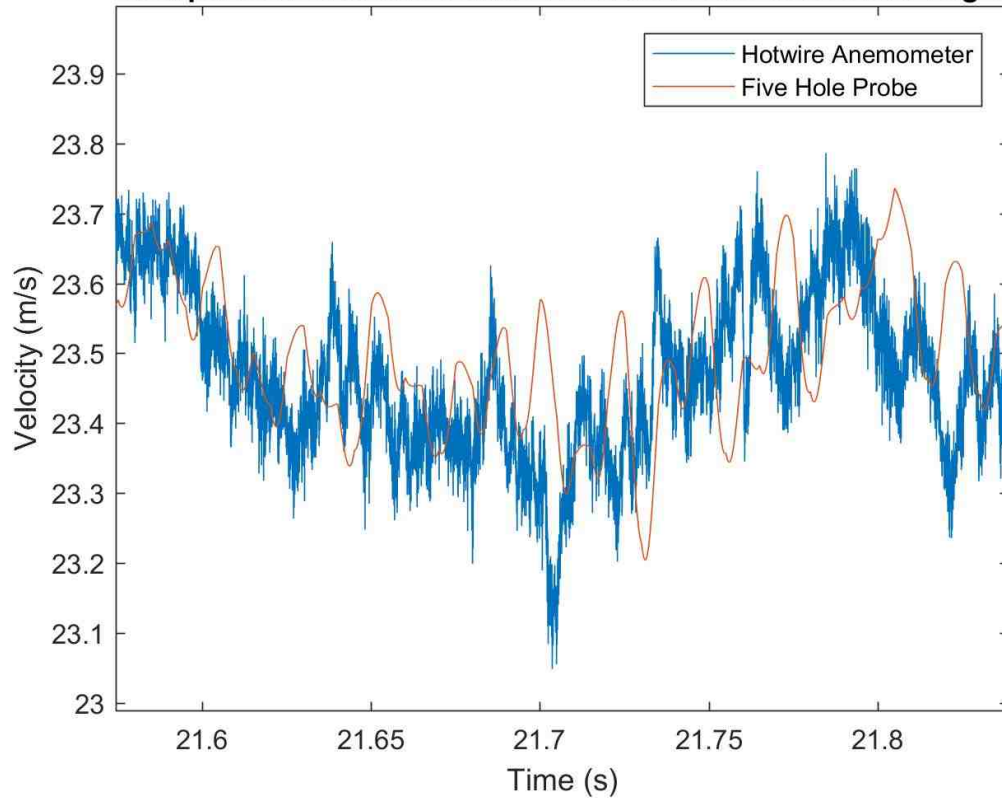
Figure 6.4: Comparison of flow speed reported by hot-wire anemometer and five hole probe zoomed in to show variation in frequency response.

Figure 6.5: hot-wire anemometer calibration: Leg 2
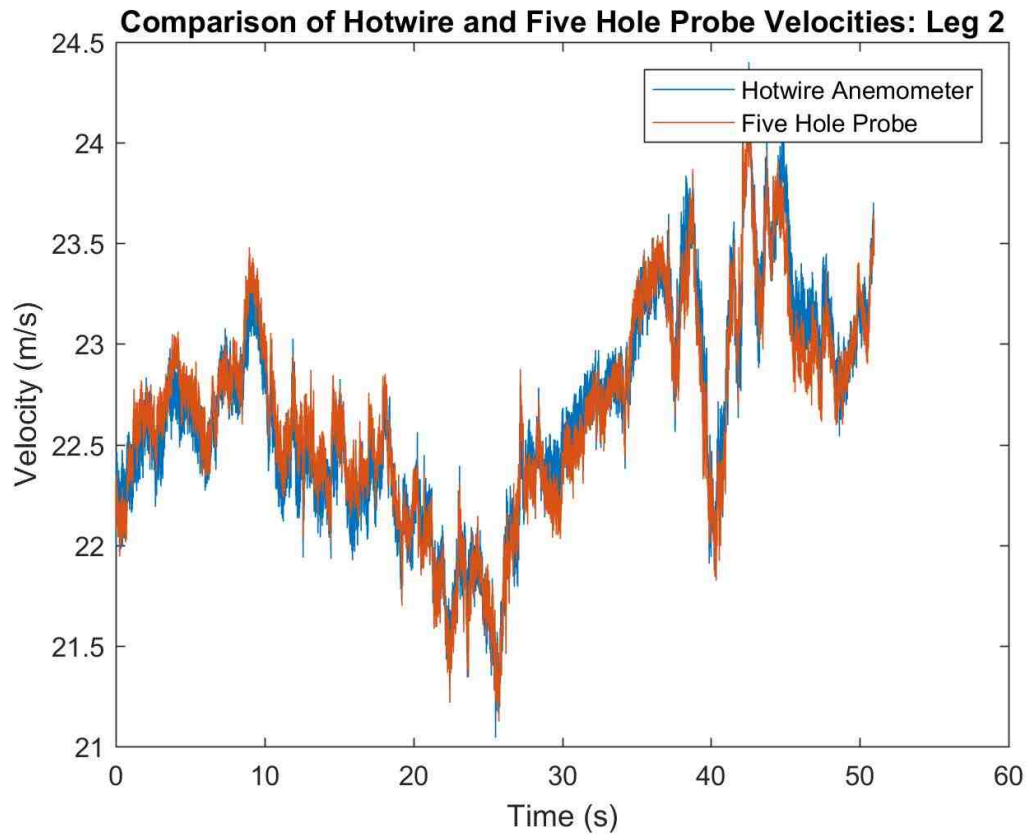
Figure 6.6: Comparison of flow speed reported by hot-wire anemometer and five hole probe

Figure 6.7: hot-wire anemometer calibration: Leg 3
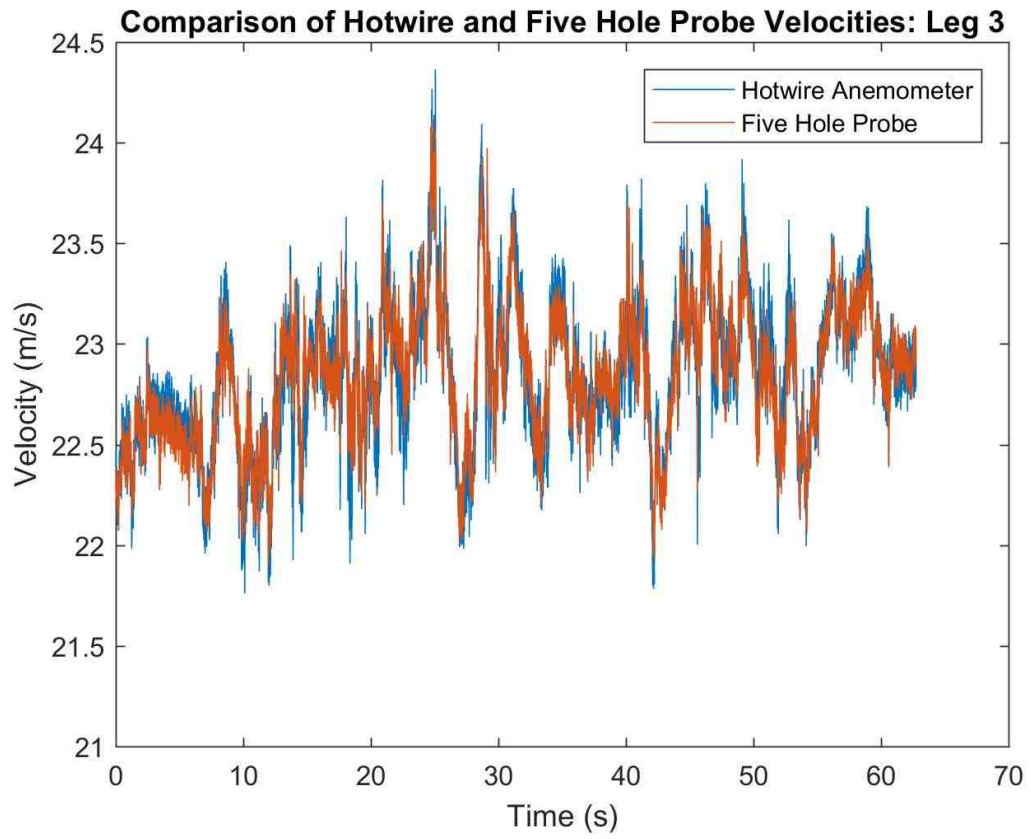
Figure 6.8: Comparison of flow speed reported by hot-wire anemometer and five hole probe
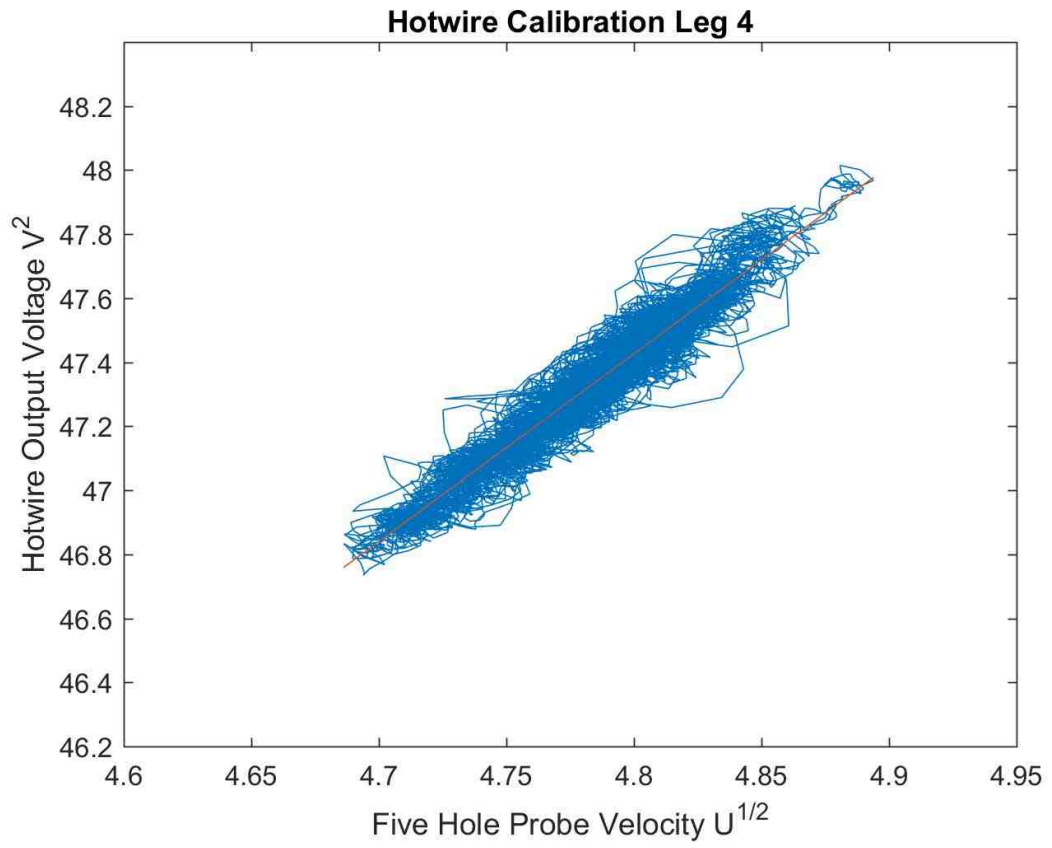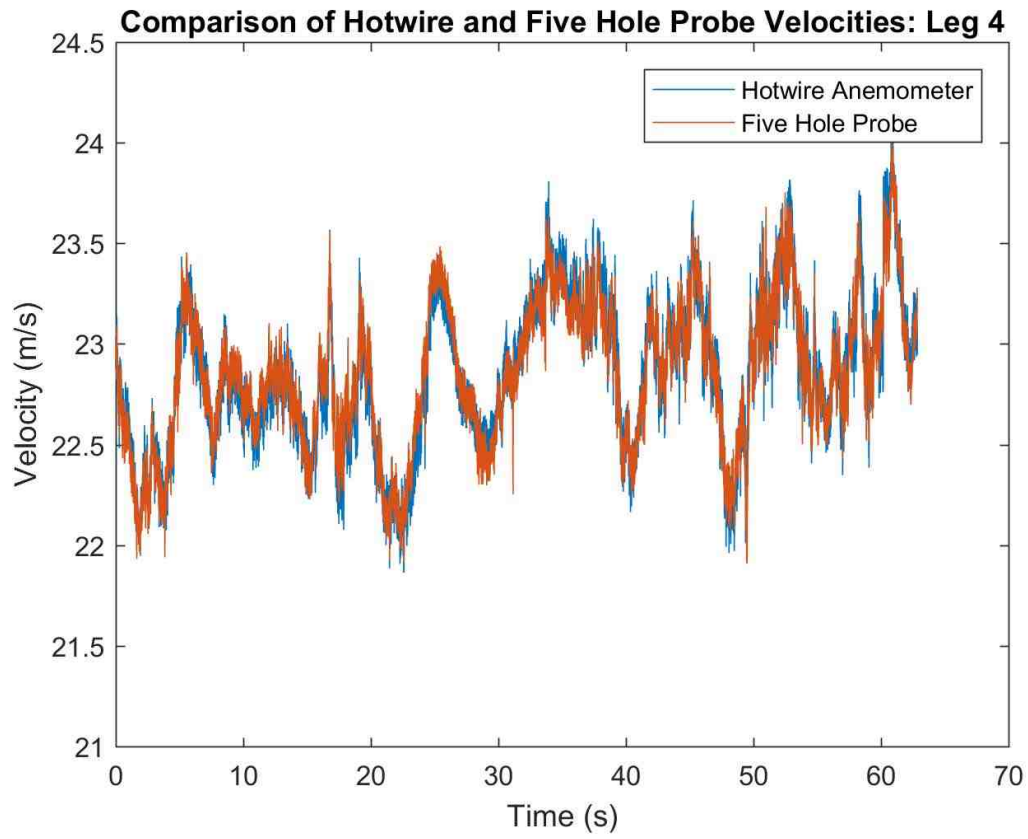
Figure 6.9: hot-wire anemometer calibration: Leg 4

Figure 6.10: Comparison of flow speed reported by hot-wire anemometer and five hole probe

6.3 Statistical Results

The general wind conditions on the day of the experiment were relatively docile, with a mean wind speed of just under 4 m/s. Figures 6.11-6.13 provide some brief insight into the mean wind and turbulent conditions during the flight experiment. Note in Figure 6.12 the increased sensitivity of the hot-wire anemometer in measuring the fluctuation velocity.
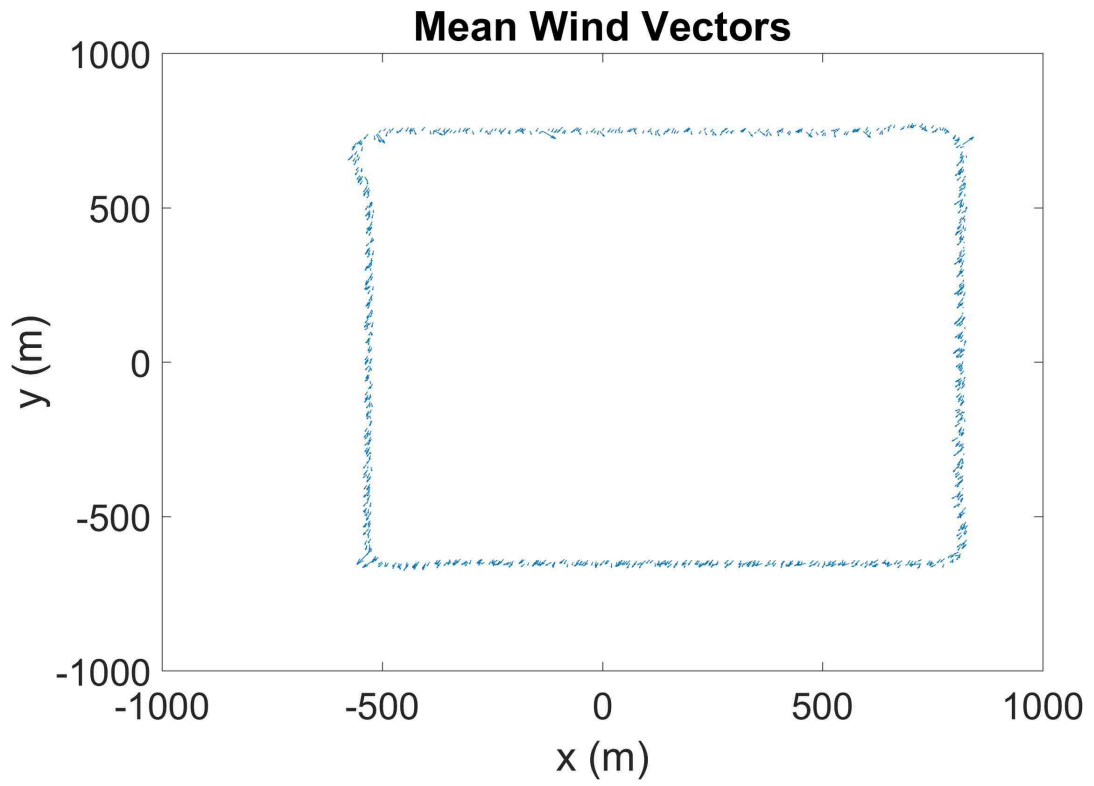
Figure 6.11: Mean wind vectors
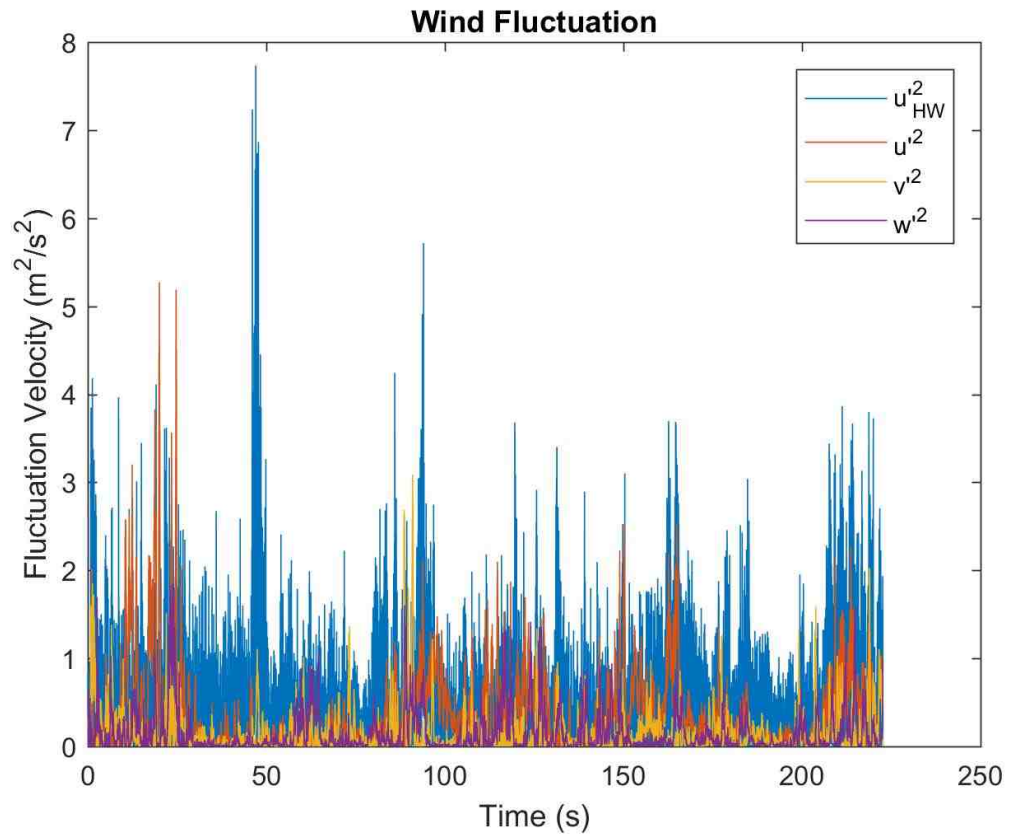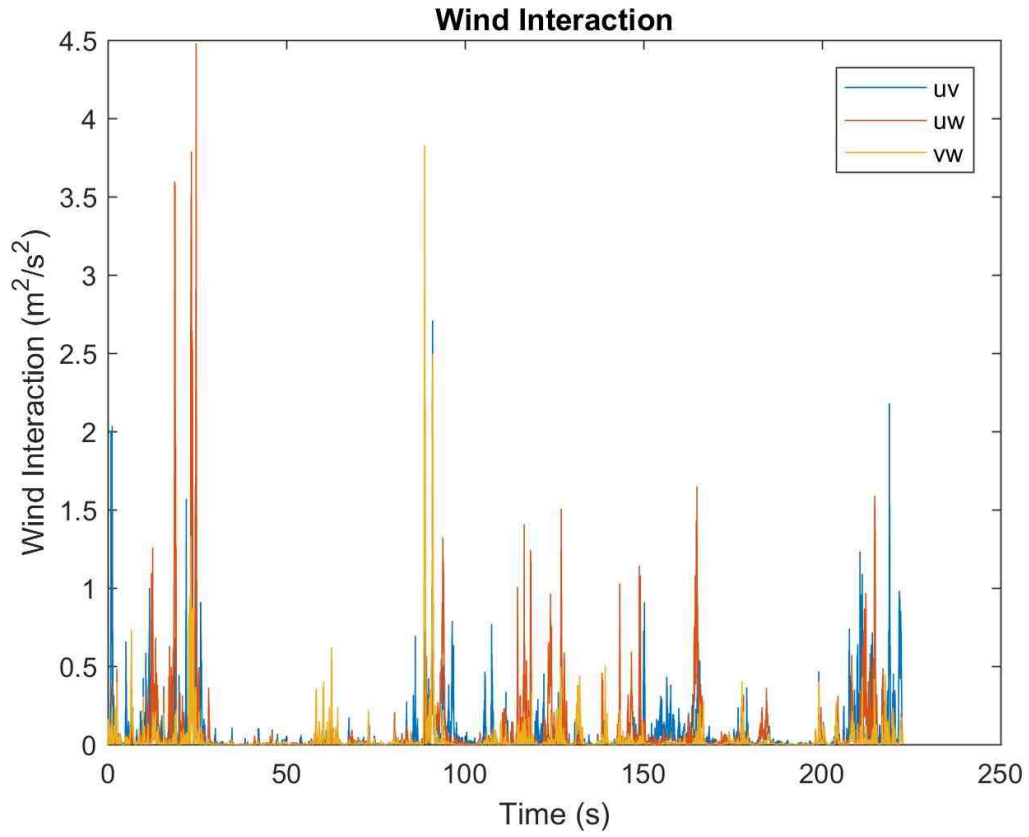
Figure 6.12: Turbulent fluctuation magnitude

Figure 6.13: Turbulence interaction magnitude

The primary goal of implementing the hot-wire anemometer was to improve the high frequency content of the acquired turbulence signal. With this improvement the vehicle is able to measure the full inertial subrange down to the dissipative range. This improved data allows for direct calculation of the instantaneous dissipation rate of the turbulence by applying the following equation.

$$\epsilon = 15\nu(du/dx)^2 \tag{6.3}$$

where the mean dissipation rate can be found by taking the time average of ϵ, or $\bar{\epsilon}$. An alternative approach to the calculation of mean dissipation rate is to use the assumed form of the inertial subrange from Kolmogorov's theory, using empirically

determined coefficients

$$\bar{\epsilon} = \overline{((P\kappa^{5/3})/0.49)^{3/2}} \tag{6.4}$$

where P is the result of the power spectrum divided by 2π and κ is the wavenumber. Calculating the dissipation rate of the turbulence in this manner is not ideal as it only allows for calculating the mean dissipation rate, while the instantaneous dissipation rate of the flow is needed to calculate several important parameters of the flow.

Figures 6.14-6.17 provide the instantaneous dissipation rate measurements calculated via equation 6.3. Be sure to note the varying scales on the vertical axis of the plots for the different legs.
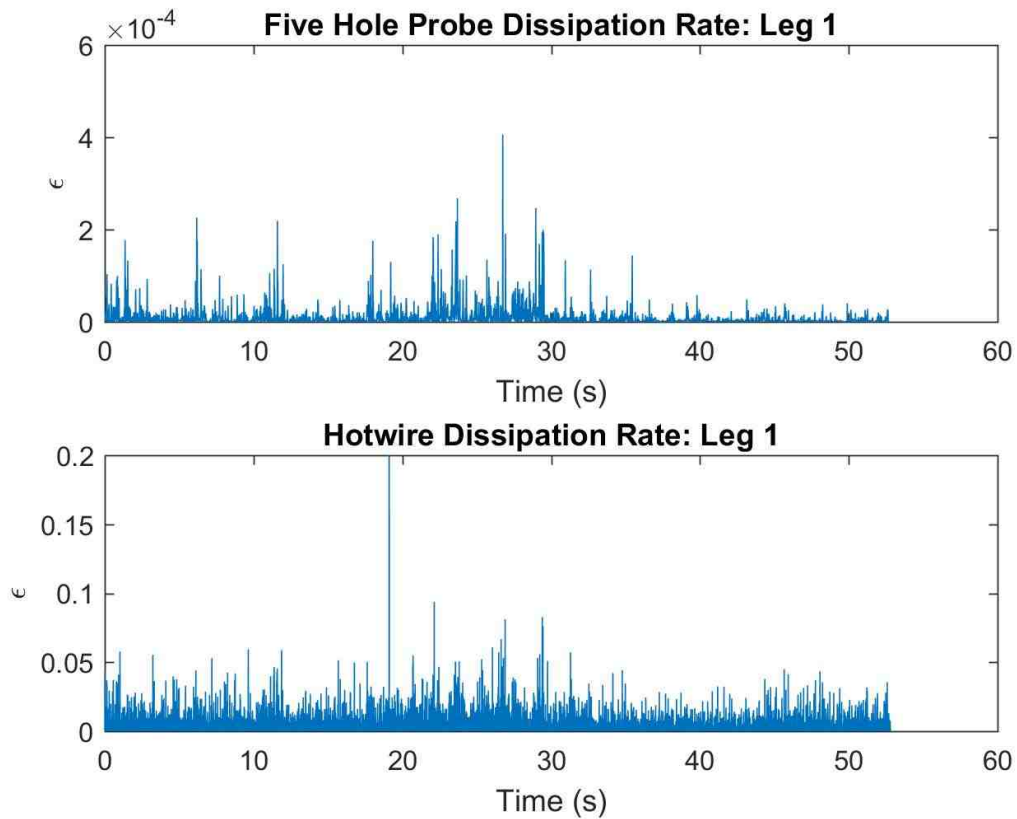

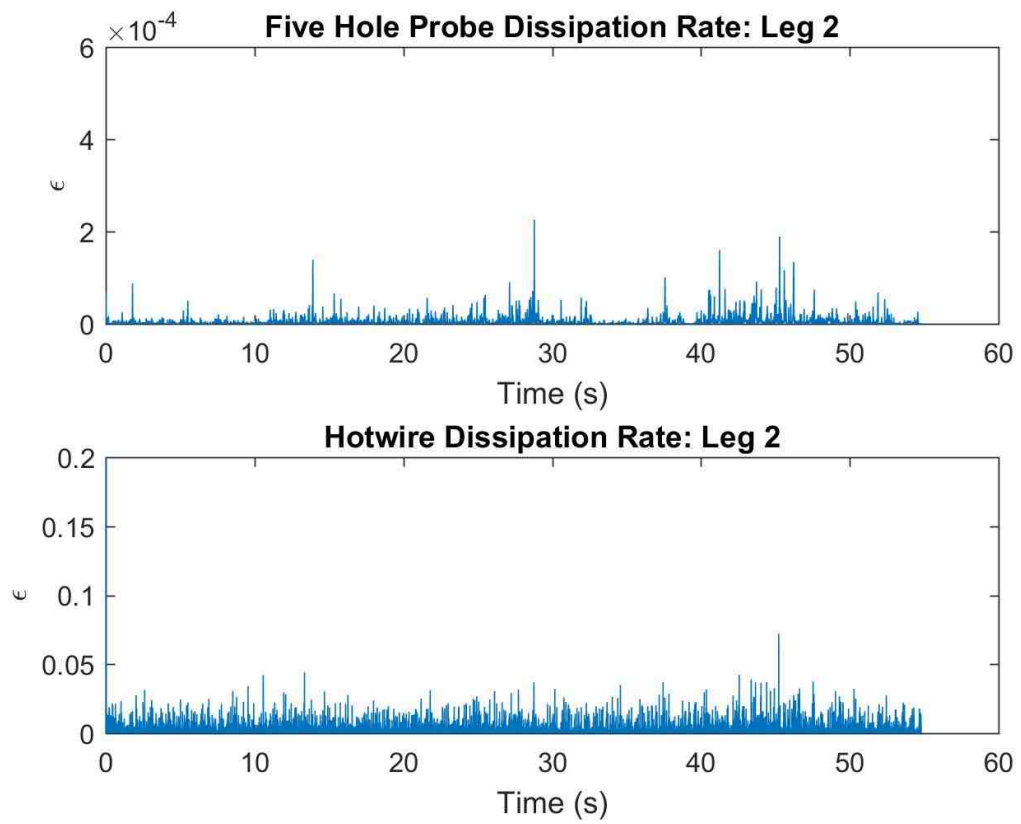Figure 6.14: Turbulence dissipation rate
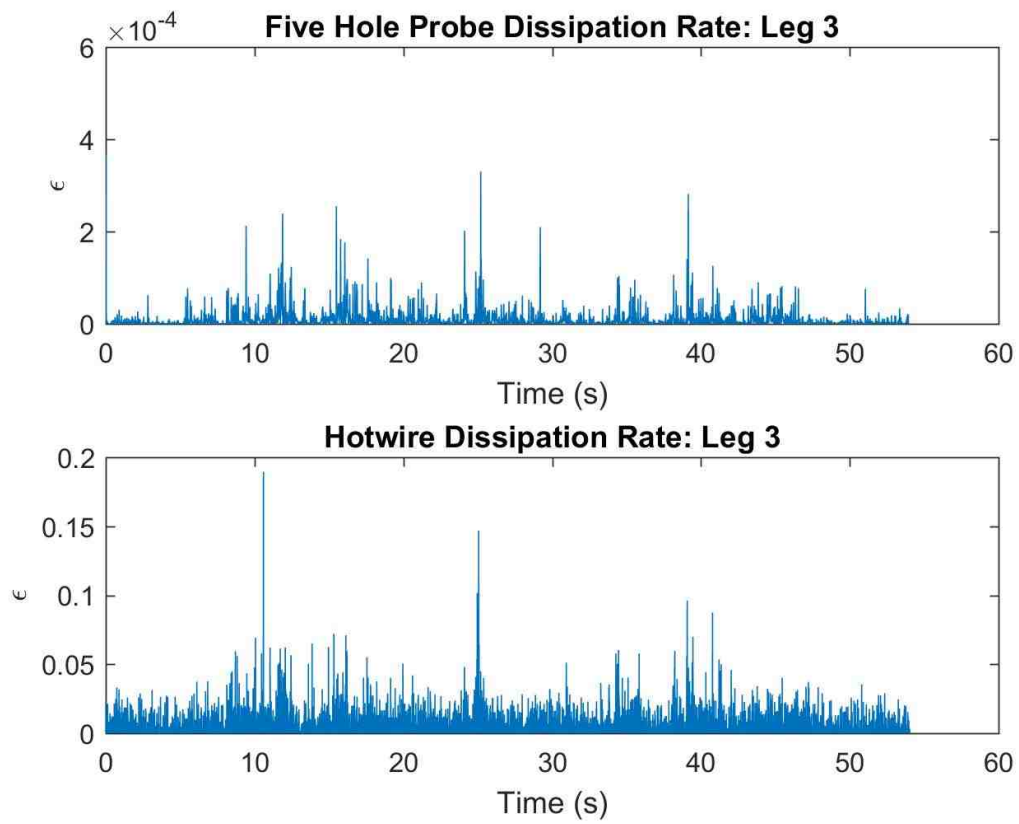
Figure 6.15: Turbulence dissipation rate

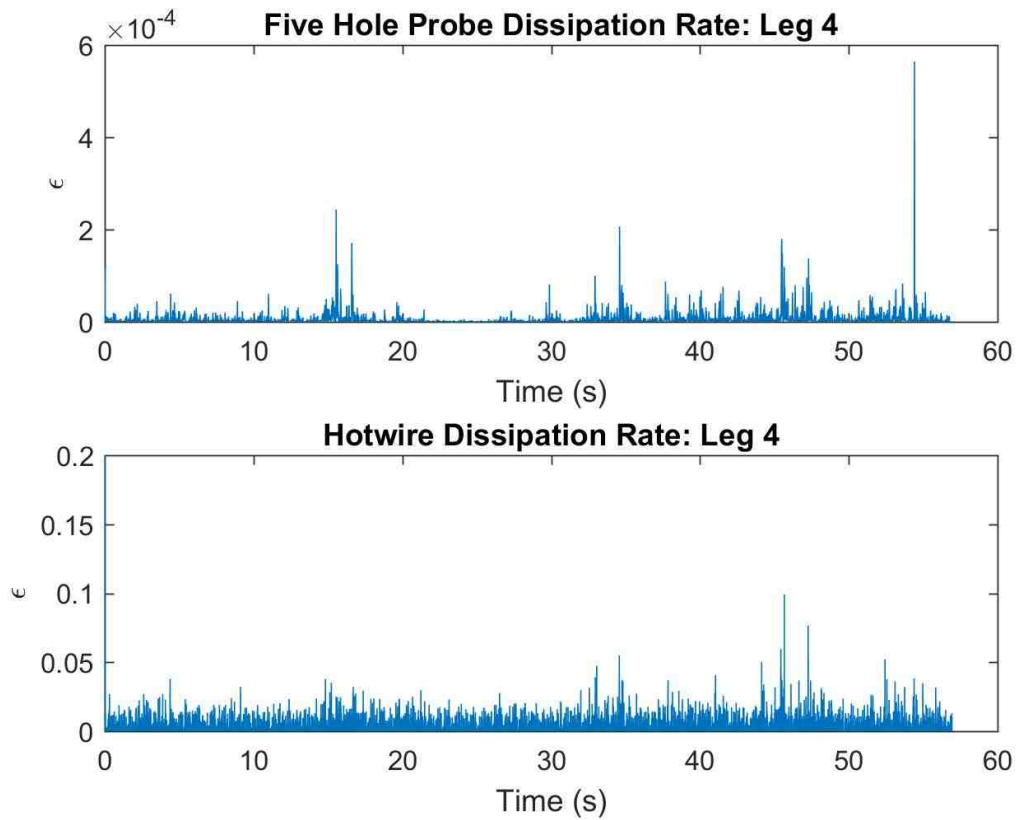Figure 6.16: Turbulence dissipation rate

Figure 6.17: Turbulence dissipation rate

Figure 6.18 demonstrates the advantage of the hot-wire anemometer over the five hole probe when attempting to determine the instantaneous dissipation rate. This plot shows that the mean dissipation rates calculated directly from the five hole probe data are extremely inaccurate. While the same calculation method applied to the hotwire anemometer data yields a result more closely matching the mean dissipation rate determined using theory.
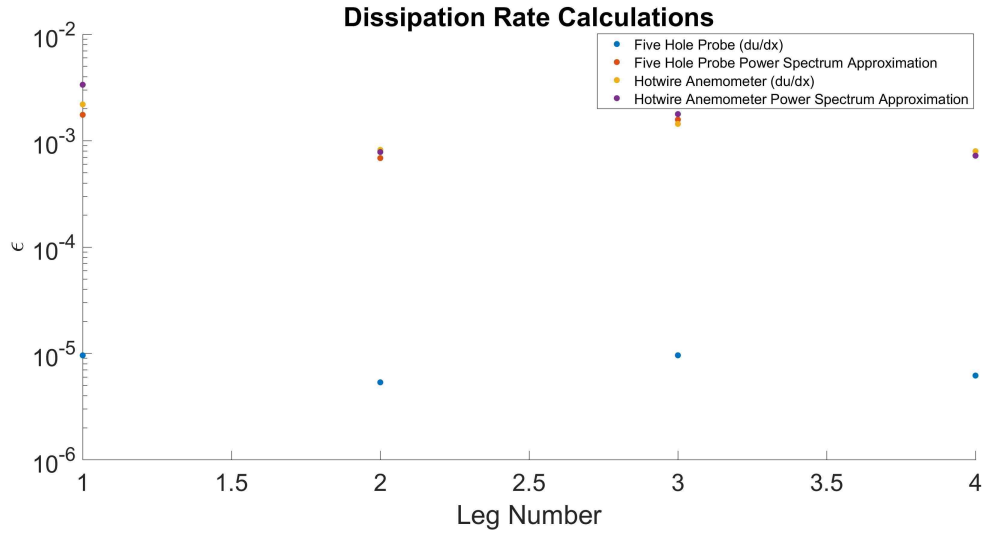
Figure 6.18: Comparison of dissipation rates

One of the most commonly used tools in characterizing a turbulent flow is the frequency spectrum. The four spectra shown in figures 6.19-6.22 clearly demonstrate the improvements made in frequency response between the five-hole probe and the hot-wire anemometer. The five-hole probe shows a bump in the spectrum at around $\kappa\eta = 0.02$, reflecting the resonance in the tubing and the upper bound in frequency resolution. Conversely, the hot-wire shows evidence of f^2 noise initiating at around $\kappa\eta = 0.3$, at least an order of magnitude higher.
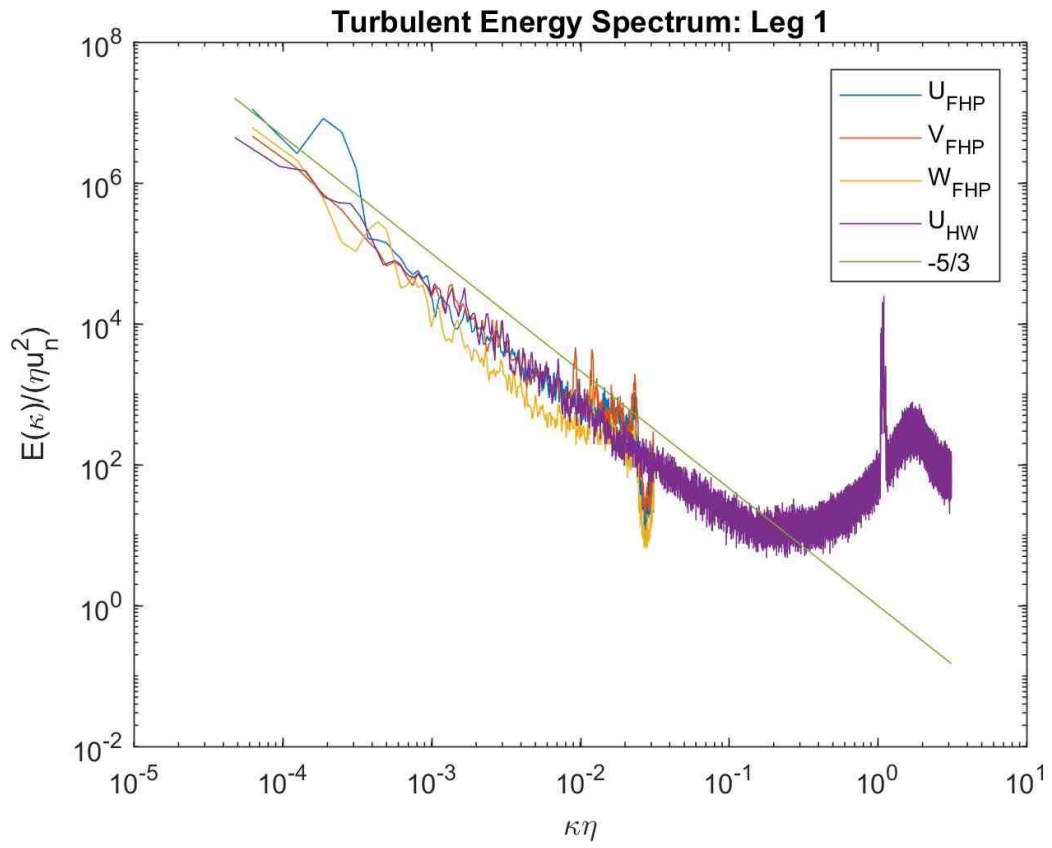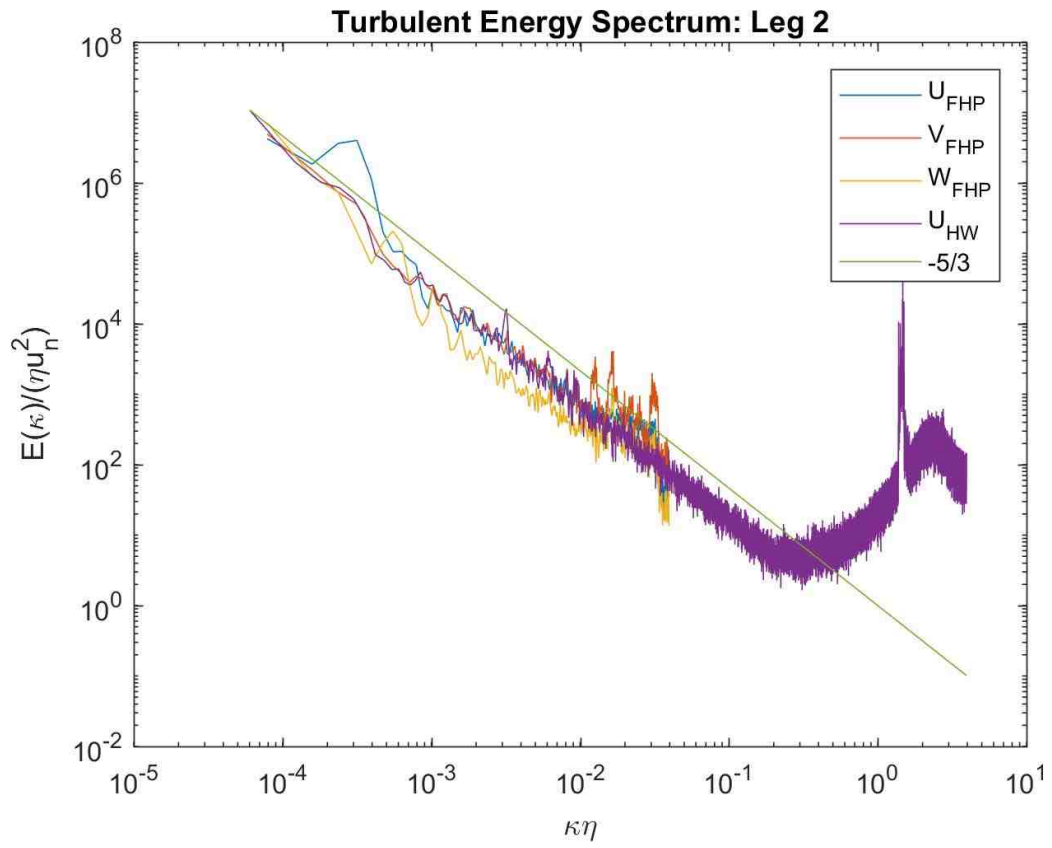
Figure 6.19: Frequency Spectrum

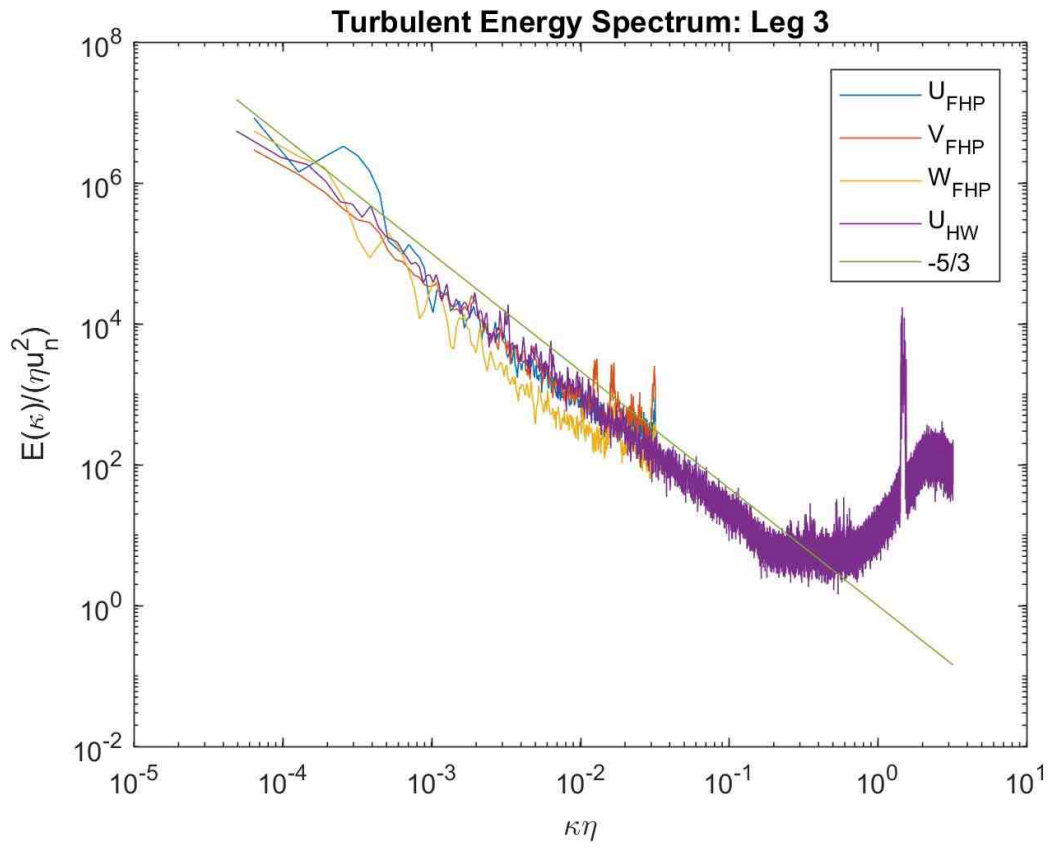Figure 6.20: Frequency Spectrum
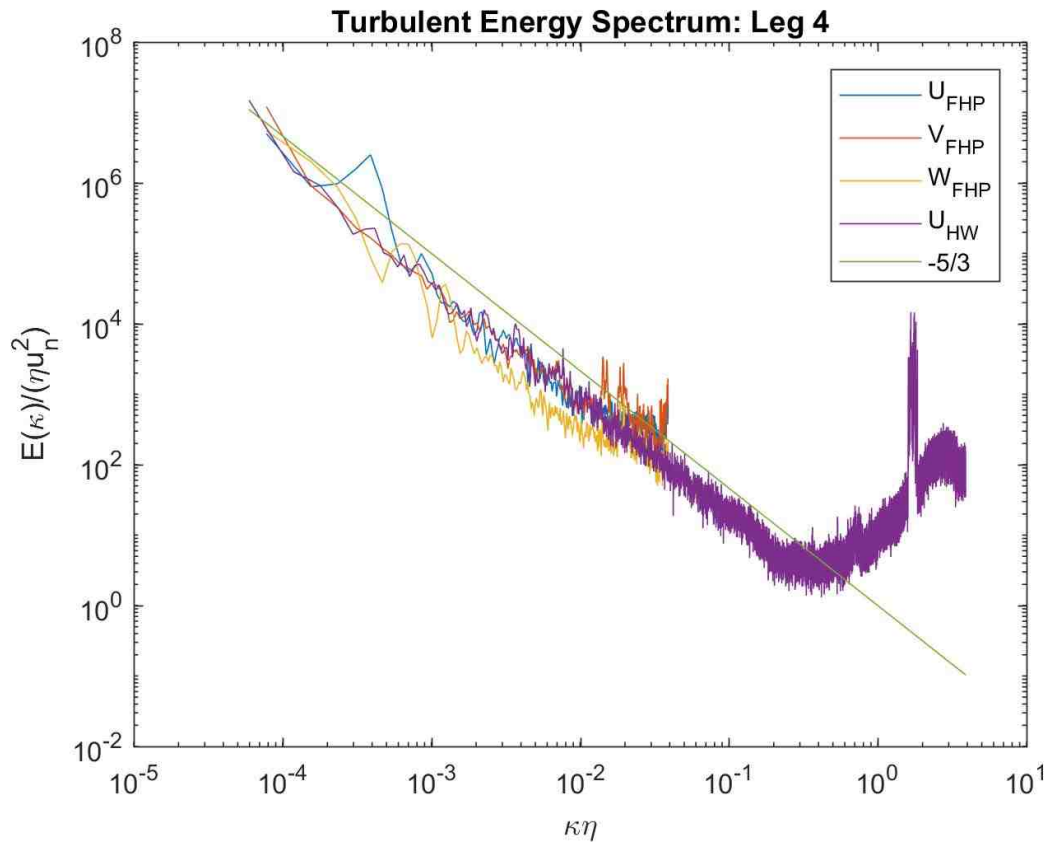
Figure 6.21: Frequency Spectrum

Figure 6.22: Frequency Spectrum

Chapter 7 Conclusions and Future Work

The BLUECAT 6B airframe was designed to collect high frequency atmospheric boundary layer turbulence data. The time response of the previous BLUECAT 5 airframe was no more than 80-100 Hz, BLUECAT 6B saw this number improved to approximately 2,000 Hz. This improved time response allows the new system to capture smaller turbulent fluctuations including the full inertial subrange down to the beginning of the dissipative range. As a result, direct calculation of the dissipation rate of the turbulence is enabled.

While the BLUECAT 6B system is fully operational and has demonstrated its ability to collect valuable turbulence data, there are still improvements that could be made. The first of these would be to eliminate sources of electromagnetic noise in the circuit. Labratory wind tunnel tests demonstrated that in ideal conditions the system is capable of operating with a time response of up to 50 kHz. Being a large electric powered dual prop airframe with powerful RF transmitters and receivers, electric noise is an obvious concern. For the initial BLUECAT 6B airframe used in this experiment some efforts were made to minimize this issue, but more effort focused on proper shielding and wire routing would likely result in further reduction of electromagnetic interference in the hot-wire circuitry.

The hot-wire anemometer offers much improved frequency response, however it does lack the ability to measure the three individual spatial components of the wind velocity. This information could be obtained by installing a three wire probe in place of the current single wire sensor. This is a long term goal as it would likely require a

larger airframe to carry the payload needed to operate three hot-wire probes.

Lastly, the hot-wire probe helps in resolving the smallest turbulent scales through its improved time response, however the largest scales of the flow will need to measured as well in order to fully characterize the flow. This issue can be resolved by modifying flight paths. The FAA currently restricts UAS operations to be within line of sight, but some progress is being made in allowing research institutions to be granted special waivers to fly beyond visual line of sight. In order to capture the largest turbulent scales the airframe will need to fly through as many of these large eddies as possible, meaning the aircraft will need to fly longer flight paths. The path flown in this experiment was as large as possible while maintaining visual line of sight. To improve this area the aircraft will either need to fly beyond visual line of sight or a ground chase vehicle will need to be employed in future missions.

Bibliography

[1] See, for example, "Deluge, a drawing by Leonardo da Vinci dating from 1511-1515, held in the Royal Library, Windsor Castle.

[2] O. Reynolds. On the dynamical theory of incompressible viscous fluids and the determination of the criterion. *PHITRA*, 186:123–164, 1895.

[3] O. Reynolds. An experimental investigation of the circumstances which determine whether the motion of water shall be direct or sinuous, and of the law of resistance in parallel channels. *Phil. Trans. R. Soc.*, 174:935–982, 1883.

[4] Cameron Tropea, Alexander L Yarin, and John F Foss. *Springer handbook of experimental fluid mechanics*, volume 1. Springer Science & Business Media, 2007.

[5] A. N. Kolmogorov. The local structure of turbulence in incompressible viscous fluid for very large reynolds numbers. *Dokl. Akad. Nauk SSSR*, 30:301–305, 1941.

[6] M. V. Zagarola and A. J. Smits. Mean-flow scaling of turbulent pipe flow. *J. Fluid Mech.*, 373:33–79, 1998.

[7] M. Hultmark, M. Vallikivi, S. C. C. Bailey, and A. J. Smits. Turbulent pipe flow at extreme reynolds numbers. *Phys. Rev. Lett.*, 108:094501, Feb 2012.

[8] B. J. Rosenberg, M. Hultmark, M. Vallikivi, S. C. C. Bailey, and A. J. Smits. Turbulence spectra in smooth- and rough-wall pipe flow at extreme reynolds numbers. *Journal of Fluid Mechanics*, 731:4663, 2013.

[9] R.B. Stull. *An Introduction to Boundary Layer Meteorology*. Springer, 1988.

[10] GARY J. KUNKEL and IVAN MARUSIC. Study of the near-wall-turbulent region of the high-reynolds-number boundary layer using an atmospheric flow. *Journal of Fluid Mechanics*, 548:375–402, 2 2006.

[11] R. M. Williams and C. A. Paulson. Microscale temperature and velocity spectra in the atmospheric boundary layer. *Journal of Fluid Mechanics*, 83:547–567, 12 1977.

[12] G. I. Taylor. The spectrum of turbulence. *Proc. R. Soc. Lond.*, 164(919):476–490, 1938.

[13] C.W. Higgins, M. Froidevaux, V. Simeonov, N. Vercauteren, C. Barry, and M.B. Parlange. The effect of scale on the applicability of taylor's frozen turbulence hypothesis in the atmospheric boundary layer. *Boundary-Layer Meteorol.*, 143:379–391, 2012.

[14] J.C. del Álamo and J. Jiménez. Estimation of turbulent convection velocities and corrections to taylor's approximation. *J. Fluid Mech.*, 640:5–26, 2009.

[15] C. M. Sheih, H. Tennekes, and J. L. Lumley. Airborne hot-wire measurements of the small-scale structure of atmospheric turbulence. *Physics of Fluids*, 14(2):201–215, 1971.

[16] Donald H. Lenschow and Warren B. Johnson Jr. Concurrent airplane and balloon measurements of atmospheric boundary-layer structure over a forest. *Journal of Applied Meteorology*, 7(1):79–89, 1968.

[17] E. N. Brown, C. A. Friehe, and D. H. Lenschow. The use of pressure fluctuations on the nose of an aircraft for measuring air motion. *Journal of Climate and Applied Meteorology*, 22(1):171–180, 1983.

[18] Wayne M. Angevine, S. K. Avery, and G. L. Kok. Virtual heat flux measurements from a boundary-layer profiler-rass compared to aircraft measurements. *Journal of Applied Meteorology*, 32(12):1901–1907, 1993.

[19] C Russell Philbrick. Raman lidar descriptions of lower atmosphere processes. *Lidar Remote Sensing in Atmospheric and Earth Sciences, Proc. 21st ILRC, Valcartier, Quebec Canada*, pages 535–545, 2002.

[20] Larry B. Cornman, Corinne S. Morse, and Gary Cunning. Cooperative forest fire surveillance using a team of small unmanned air vehicles. *International Journal of Systems Science*, 32(1):171–177, 2006.

[21] F. R. Payne and J. L. Lumley. One-dimensional spectra derived from an airborne hot-wire anemometer. *Quarterly Journal of the Royal Meteorological Society*, 92(393):397–401, 1966.

[22] Brandon M Witte. Development of an unmanned aerial vehicle for atmospheric turbulence measurement. 2016.

[23] Brandon Witte, Robert Singler, and Sean Bailey. Development of an unmanned aerial vehicle for the measurement of turbulence in the atmospheric boundary layer. *Atmosphere*, 8(10):195, 2017.

[24] Timothy Bonin, Phillip Chilson, Brett Zielke, and Evgeni Fedorovich. Observations of the early evening boundary-layer transition using a small unmanned aerial system. *Boundary-Layer Meteorology*, 146(1):119–132, 2013.

[25] Jamey Jacob, Phillip Chilson, Adam Houston, and Suzanne Smith. Considerations for atmospheric measurements with small unmanned aircraft systems. *Atmosphere*, 9(7):252, 2018.

[26] Benjamin Hemingway, Amy Frazier, Brian Elbing, and Jamey Jacob. Vertical sampling scales for atmospheric boundary layer measurements from small unmanned aircraft systems (suas). *Atmosphere*, 8(9):176, 2017.

[27] Dale A Lawrence and Ben B Balsley. High-resolution atmospheric sensing of multiple atmospheric variables using the datahawk small airborne measurement system. *Journal of Atmospheric and Oceanic Technology*, 30(10):2352–2366, 2013.

[28] S. Tavoularis. *Measurement in Fluid Mechanics*. Cambridge University Press, 2005.

[29] N. Wildmann, S. Ravi, and J. Bange. Towards higher accuracy and better frequency response with standard multi-hole probes in turbulence measurement with remotely piloted aircraft (rpa). *Atmospheric Measurement Techniques*, 7(4):1027–1041, 2014.

[30] Weather prediction by numerical process. by lewis f. richardson. cambridge (university press), 1922. 4. pp. xii + 236. 30s.net. *Quarterly Journal of the Royal Meteorological Society*, 48(203):282–284, 1922.

[31] U. Frisch. *Turbulence: The Legacy of A. N. Kolmogorov*. Cambridge University Press, 1995.

[32] A. N. Kolmogorov. A refinement of previous hypotheses concerning the local structure of turbulence in a viscous incompressible fluid at high reynolds number. *Journal of Fluid Mechanics*, 13(1):8285, 1962.

[33] S. G. Saddoughi and S. V. Veeravalli. Local isotropy in turbulent boundary layers at high reynolds number. *J. Fluid Mech.*, 268:333–372, 1994.

[34] M. V. Zagarola. *Mean-Flow Scaling of Turbulent Pipe Flow*. PhD thesis, Princeton University, 1996.

[35] S. C. C. Bailey and A. J. Smits. Experimental investigation of the structure of large- and very-large-scale motions in turbulent pipe flow. *J. Fluid Mech.*, 651:339–356, 2010.

[36] M. Vallikivi, M. Hultmark, S. C. C. Bailey, and A. J. Smits. Turbulence measurements in pipe flow using a nano-scale thermal anemometry probe. *Exp. Fluids*, 51:1521–1527, 2011.

[37] L. Barbieri et al. Small unmanned aircraft systems (sUAS) in atmospheric science: Measurement intercomparison for LAPSE-RATE. *Sensors (in review)*, 2019.

[38] H. H. Bruun. *Hot-wire Anemometry.* Oxford University Press, Oxford, UK, 1995.

[39] J. P. Monty. *Developments in Smooth Wall Turbulent Duct Flows.* PhD thesis, University of Melbourne, 2005.

[40] S. G. Saddoughi and S. V. Veeravalli. Hot-wire anemometry behaviour at very high frequencies. *Meas. Sci. Technol*, 7:1297–1300, 1996.

Vita

Caleb Alan Canter

Education

- Master of Science in Mechanical Engineering at the University of Kentucky, May 2017 - Present.

- Bachelor of Science in Mechanical Engineering at the University of Kentucky (May 2017).

- Department of Mechanical Engineering Aerospace Certificate.

Employment

- Project Engineer, Kinemetrix (September 2018 - Present); Lexington, KY. Responsibilities include: Writing robot and PLC programs, developing vision applications, and developing new technologies.

- Systems Engineering Student Tech, Lockheed Martin Missiles and Fire Control (January 2016 - December 2016); Lexington, KY. Responsibilities include: Writing integration test plans, facilitating test efforts, and tracking requirements fulfillment.

- Manufacturing Engineering Intern, GE Power and Water (Summer 2015); Greenville, SC. Responsibilities include: developing tool kitting procedures, integrating

lathe to reduce cycle delays, maintain and facilitating repairs for hydraulic float units.

- Private Contractor AutoCAD, Adam's Magnetic (August 2014 - December 2016). Resposibilities include: Creating 2D part drawings of all magnetic products.

- Lab Technician, University of Kentucky Unmanned Systems Lab (August 2013 - August 2018); Lexington, KY. Responsibilities include: Design and assemble various research airframes and instrumentation systems, plan and facilitate test flights, and train undergraduate students in lab operations.